

A New Path Forward for Understanding Microstructural Evolution during Welding

In-situ X-ray probing of welds was developed using synchrotron radiation for the direct observation of phase transformations during welding

BY JOHN W. ELMER

ABSTRACT. Over the past century, the principal method for estimating the sequence of microstructural events that produce the final weld microstructure has been postweld microstructure analysis, and it's the interpretation of these microstructures that sets welding metallurgy apart from other related endeavors. In conjunction with heat flow analysis and thermodynamic principles, the postweld microstructural interpretation of grain sizes and shapes, second-phase particles, interphase boundaries, and composition gradients provide the framework for interpreting the events that lead to the final microstructure. However, without direct and confirming evidence of the actual phases that exist during welding, multiple interpretations for microstructural evolution of welds often occur. For this reason, methods for the direct observation of the phases and phase transformations that occur during welding was developed. This paper summarizes the 2007 Adams Lecture titled "A New Path for Understanding Microstructural Evolution during Welding Using Synchrotron Radiation," where real-time X-ray diffraction methods were presented as a means for the direct observation of phase transformations during welding.

A Brief History of Synchrotron Radiation

Synchrotron radiation is a form of electromagnetic radiation that is emitted by charged particles moving in a curved path. As the charged particles accelerate around the path, they emit energy tangent to the curved path with wavelengths that cover a broad spectral range extending from the infrared to hard X-ray portions of the electromagnetic spectrum (Refs. 1-3). These X-rays are often generated in

facilities specifically designed to produce intense and highly collimated X-ray beams for the purpose of performing controlled scientific experiments. The power of synchrotron radiation is that it is both tunable in wavelength and intensity. These parameters are controllable and are related to the energy of the charged particle, the radius of the curved path, and the number of charged particles in the circulating beam. Synchrotron design takes advantage of these parameters by developing large storage rings targeted to perform specific types of experiments, for example soft or hard X-ray applications, that can be operated around the clock. The high intensity and broad spectrum of synchrotron radiation has enabled it to become one of the most important research tools for the study of matter in all its various forms, and can be used as a non-contact probe to determine the otherwise invisible structure of matter.

The roots of synchrotron radiation trace back to the invention of X-ray tubes in the late 1800s. The historical development of synchrotrons and X-rays is a fascinating one involving some of the great names in science and many Nobel prizes (Refs. 4, 5). The first Nobel Prize in Physics was given to W. Röntgen for the discovery of X-rays in 1901, which created an intense competition for further discoveries and new applications. Vacuum X-ray tubes were soon developed and optimized to generate higher-intensity X-ray beams for physics experiments. X-ray tubes gave

way to cyclotrons as a means to create higher-energy electron interactions, and this eventually led to the discovery of synchrotron radiation in 1947 when visible light was observed emanating from a 70-MeV beam being used in a cyclotron experiment at General Electric's Schenectady facility (Refs. 2, 3, 6). Within the next decade synchrotron radiation was being studied on larger and larger cyclotrons, and experiments were being performed using the synchrotron as a soft X-ray source. By the early 1960s, the first-generation synchrotrons were being built around the world with GeV energies to access the hard X-ray spectrum for solid-state technology research.

The earliest first-generation synchrotrons were called parasitic facilities because they were built as part of high-energy physics studies that were not devoted solely to the generation of synchrotron radiation (Ref. 1). However, the demand for access to synchrotron beam time was high and facilities were being proposed to be devoted to synchrotron radiation research. By the mid 1960s, the first storage rings were being built, which allowed electrons or positrons to be circled under high-vacuum conditions for extended periods. These storage rings permitted multiple beam lines to access high flux synchrotron radiation for many hours at a time. In 1974, the first storage ring in the multiple GeV range providing hard X-rays to a large community of users was built at the Stanford Linear Accelerator Center (SLAC), in Palo Alto, Calif. (Ref. 1). The 2.5-GeV SPEAR ring at SLAC included five experimental stations and was being used for more than just high energy physics experiments. However, SPEAR was still a parasitic ring at the time and didn't operate at optimum conditions for many of the types of experiments that synchrotron researchers were interested in.

The second-generation synchrotron storage rings were built in the late 1970s and early 1980s, and around that time

KEYWORDS

HAZ Formations
In-Situ Experiments
Microstructure Evolution
Phase Transformations
Real Time Observations
Synchrotron Radiation
Solidification Mode
X-Ray Diffraction

JOHN W. ELMER is Group Leader, Materials Joining, Materials Science and Technology Div., Lawrence Livermore National Laboratory, Livermore, Calif. This is the Adams Lecture presented at the 2007 AWS Meeting, Chicago, Ill.

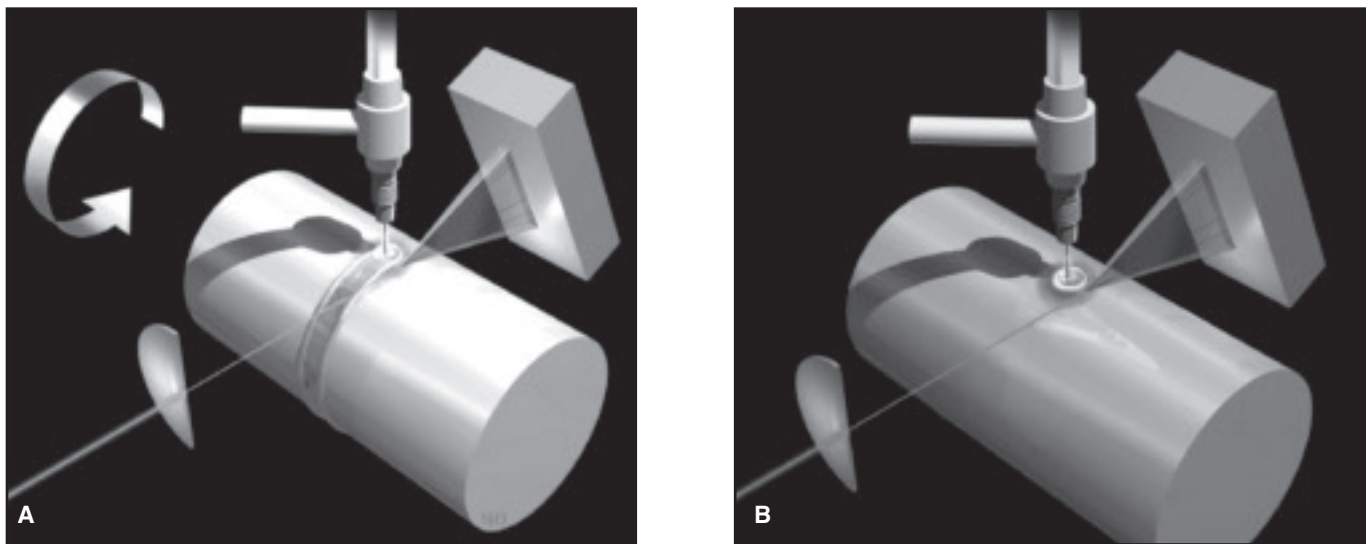


Fig. 1 — Illustrations of the following: A — SRXRD experimental setup where a steady-state weld is made by rotating the bar being welded beneath a stationary torch; B — TRXRD experimental setup where a transient GTA spot weld is made on top of a stationary bar. In both cases, the synchrotron beam (already focused and monochromatized) enters from the left and passes through a pinhole to provide spatial resolution. The X-ray detector is illustrated downstream of the weld to collect the diffracted beams.

some of the original first-generation sources were converted to second-generation sources (Refs. 1, 2). The second-generation storage rings were designed and dedicated to synchrotron radiation studies, and were finding an increasing number of applications. Whereas previous generation machines were largely used for physics research, the second generation sources were finding large numbers of users in more diverse fields such as chemistry, biology, geology, and engineering. High-flux experiments were possible on these beam lines using magnetic bending devices and other insertion devices (Refs. 1–3, 6, 7), allowing spatially resolved and time-resolved experiments to be performed at levels not possible using conventional X-ray sources.

As the demand for these types of experiments increased, it was clear that beam brightness was becoming as important, and sometimes more important, than beam flux. Brightness is a property of the beam defined as the number of photons emitted per second, per square millimeter, per square milliradian of opening angle within a given spectral bandwidth, usually 0.1% (Ref. 1). The brightness of the second-generation sources was increased, and at the same time beam wigglers and undulators (Refs. 1–3, 6, 7) were being developed that produced beams with even higher brightness. These beams were allowing developments to be made in the fields such as angular resolved photoemission for the study of electronic structure of solids and surfaces, extended X-ray absorption fine-structure spec-

troscopy (EXAFS) for measurement of local atomic structure, protein crystallography, X-ray lithography, and topography (Refs. 1–3, 6, 7).

The third-generation, and most recent, synchrotron sources are built as fully dedicated facilities with high brightness and high flux capabilities in mind. Smaller third-generation sources such as the Advanced Light Source (ALS) in Berkeley, Calif., were developed for VUV and soft X-ray production and have circumferences on the order of 200 m. Larger third-generation sources such as the Advanced Photon Source (APS), located at Argonne National Laboratory near Chicago, Ill., or the European Synchrotron Radiation Facility (ESRF), located in Grenoble, France, which have circumferences on the order of 1000 m, were developed primarily for the hard X-ray spectrum. These third-generation sources are distinguished from second-generation sources in that they have higher inherent brightness and were designed specifically for the insertion of beam-enhancing devices to further increase their flux and brightness. There are more than 20 of these third-generation sources in more than 10 countries throughout the world today (Ref. 1), with multiple thousands of users running experiments each year. Whereas the early synchrotron sources were only being used for high energy physics experiments, the access to the new third generation sources are available to all scientific and engineering endeavors. Many synchrotrons are user facilities that are open to all types of researchers, oftentimes through an open proposal competition process.

The Application of Synchrotron Radiation to Welding

A project was initiated at Lawrence Livermore National Laboratory (LLNL) in 1993 to investigate the feasibility of using synchrotron radiation as an *in-situ* probe to investigate phase transformations that occur during welding. Because of its intense and highly collimated X-ray beams, it was believed that atomic structure of welds could be probed in real time with sufficient temporal and spatial resolution to gather meaningful data about the phase transformations that occur during welding. This feasibility study led to three early publications that demonstrated that a spatially resolved X-ray beam produced at SSRL could be used for the *in-situ* identification of high-temperature phases in the heat-affected zone (HAZ) of welds (Refs. 8–10). Based on this early work, a program was initiated by the Department of Energy's Office of Basic Energy Science to study the kinetics of phase transformations during welding using *in-situ* synchrotron radiation as a real-time X-ray probe. This larger program was funded at LLNL from 1996 through 2004, where direct observations of welding-induced phase transformations were performed on many different metals and alloys at SSRL as is discussed in more detail later. From 2005 to the present, additional synchrotron-based work is being performed at APS where a weld simulation technique is used rather than direct welding to allow solid-state phase transformations to be studied under more controlled conditions. This paper provides an overview of the work

that has been done to date at LLNL at both the SSRL and the APS synchrotron facilities.

Introduction

The need for *in-situ* observations of phase transformations during welding stems from the fact that very little unequivocal data are available about the phases that exist in the extreme conditions that surround welds. Experimental observations are hampered by the severe temperature gradients, high peak temperatures, and rapid thermal fluctuations that occur in the weld HAZ. Although the resulting effects of weld temperatures on weld microstructures are well known (Refs. 11–13), the lack of actual data acquired during welding has severely limited the validation of the theories and models that have been proposed for the evolution of weld microstructure. Unlike postweld metallographic observations, which are essentially postmortem examinations of the weldment, synchrotron observations allow the phase transformations to be directly observed in realtime with high spatial resolution for actual verification of the phases that exist.

In-situ synchrotron X-ray diffraction methods are direct, in that they can determine the actual phases that exist during welding. If a high-temperature phase is identified by its X-ray diffraction pattern, then it is certain that that phase was present. This fact is one of the principal distinctions between synchrotron observations and other methods for weld microstructure analysis. Conventional, indirect methods measure some property of the metal or alloy (length, resistivity, enthalpy) during simulated weld heating and cooling, but do not verify the presence or absence of a given phase as transformations occur. For example, high-temperature dilatometry or gleeble testing, measures the change in length of a sample during heating and cooling, but the phases that are really present can only be inferred from the results. Complex phase transformations and those involving substantial changes in composition due to chemical diffusion cloud the picture of what is really taking place. Similar complications arise when trying to interpret differential scanning calorimetry data (changes in enthalpy), or resistivity data (changes in electrical properties) during thermal cycling.

Although the heating cycle of the weld can be modeled and/or experimentally measured, the kinetics of each of the various phase transformations are difficult to determine and are rarely known under actual welding conditions. In the absence of these data, isothermal time-temperature-transformation (ITT) and continuous-cool-

ing-transformation (CCT) diagrams, which are available for many ferrous and non-ferrous alloys (Refs. 14, 15), are sometimes used to approximate the behavior of phase transformations that occur during the non-isothermal cooling cycle of the HAZ (Ref. 12) if the thermal profile of the weld is known. Application of these diagrams for the prediction of weld behavior requires many assumptions in order to deal with the nonuniform temperature distribution of welds (Ref. 12). Furthermore, these diagrams represent the cooling but not the heating portions of the HAZ, and there is no generally accepted method for verifying how well these diagrams predict actual HAZ behavior. This lack of information has hindered both the efforts to develop

comprehensive models for the prediction of the HAZ microstructure, and our basic understanding of microstructural evolution in welds.

Even if kinetic data were available, the temperature cycle of the weld has to be known in order to properly predict the effects of welding on microstructure. Since it is extremely difficult to get reliable experimental thermal data from welds, numerical modeling of the weld temperatures is now being used to determine the weld thermal cycles. These numerical models have advanced considerably (Refs. 16–22) over the analytic solutions to weld heat flow that were prominent two decades ago (Ref. 12). Numerical weld models are now being used by weld researchers to calculate the size and shape of the fusion zone with three-dimensional coupled thermal fluid codes for quasi-steady-state welds (Refs. 23, 24), as well as the more complicated transient welds (Refs. 25–27). The resulting calculations allow the spatial distribution of peak temperatures, heating rates, and cooling rates in the HAZ to be determined. However, without corresponding phase transformation kinetic data, microstructural evolution in the weld HAZ cannot be predicted.

Obtaining kinetic data about phase



Fig. 2 — Photograph of an SRXRD experiment in progress in the experimental hutch at beam-line 10-2 at SSRL. An aluminum environmental chamber surrounds the weld and X-ray detector. The welding arc is visible as a blue glow seen through the same port where the synchrotron beam enters the side of the chamber. An infrared camera views the weld through a second port located on the top of the chamber.

transformations in welds is complicated by the intense thermal conditions surrounding welds that interfere with all types of physical probes that are placed near them. Because of this, a noncontact probe was desired that could identify phases during welding with high spatial resolution and would not be damaged by the welding arc. Synchrotron radiation turned out to be ideal for this probe, and two synchrotron-based techniques were developed at Lawrence Livermore National Laboratory specifically aimed at gathering realtime phase transformation data from welds. These techniques are referred to as spatially resolved X-ray diffraction (SRXRD) and time-resolved X-ray diffraction (TRXRD). In addition, a weld simulation technique was developed for direct observations of phase transformations under controlled heating and cooling (CHC) conditions. These three techniques are new to welding and permit 1) the direct observation of the solidification mode of an alloy during welding, 2) the ability to discover, in real time, definitive sequence of phase transformations that lead to the final weld microstructure, and (3) the capability to generate quantitative kinetic data of phase transformations

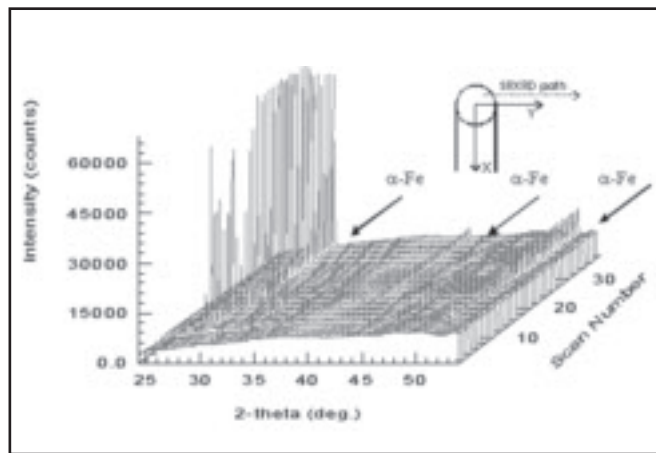
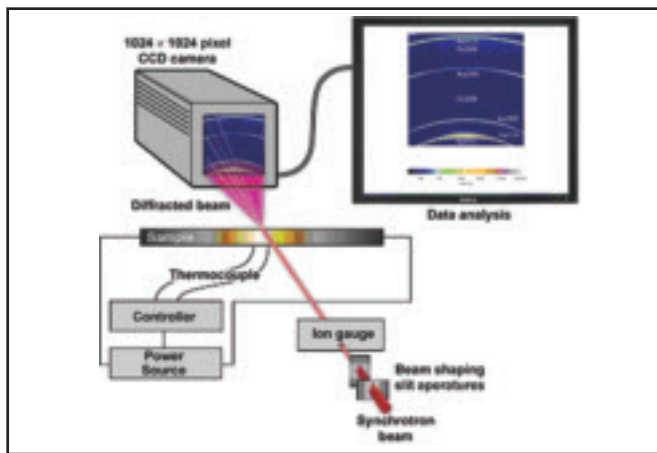


Fig. 3 — Schematic diagram of the X-ray setup used for in-situ observations of phase transformations under controlled heating and cooling (CHC) conditions. The synchrotron beam passes through vertical and horizontal slits for spatial resolution, and the sample is heated by a direct resistance method. An environmental chamber (not illustrated) surrounds the sample to prevent oxidation during the run.

Fig. 4 — A typical complete SRXRD scan showing 37 diffraction patterns taken across the weld HAZ. The schematic drawing illustrates the scan path of the beam. Each successive diffraction pattern was taken at 0.25-mm steps along the y direction away from the weld centerline. The α -ferrite peaks are indicated, the remaining peaks correspond to those of γ -austenite.

through synthesis of *in-situ* data with the temperature history obtained through numerical heat transfer modeling. From these data, the kinetics of phase transformations that occur under the highly non-isothermal heating and cooling cycles produced during welding can be better understood. This paper presents an overview of each technique and some of the experimental highlights that each has produced.

In-Situ Synchrotron Experimental Methods and Modeling

Spatially Resolved X-Ray Diffraction (SRXRD)

The SRXRD technique was the first method developed at LLNL to observe phase transformations during welding, and is used to both identify and map phases that exist in the heat-affected zone (HAZ) of steady-state moving arc welds. In this method, X-ray diffraction patterns are acquired in real time at discrete locations in the weld HAZ (Refs. 28–36). This data can be further analyzed and modeled to understand the kinetics of phase transformations taking place (Refs. 37–45). Figure 1A shows a schematic illustration of the SRXRD technique, where a steady-state gas tungsten arc (GTA) weld is made by rotating a metal bar at a constant speed beneath the welding torch, while the spatially resolved synchrotron beam is used to probe the phase present in the weld HAZ (Refs. 28, 29).

All of the SRXRD experiments on welds were performed on the 31-pole wiggler beam line, BL 10-2 (Ref. 46) at SSRL with SPEAR (Stanford Positron-Electron

Accumulation Ring) operating at an electron energy of 3.0 GeV and an injection current of ~ 100 mA. These experiments used a synchrotron beam that emerged from the wiggler and was focused by a toroidal mirror back to the source size of $\sim 1 \times 2$ mm before being monochromatized using a double Si (111) crystal. After leaving the monochromator, the beam is spatially resolved by passing it through a tungsten pinhole with diameters 180 μ m, 260 μ m, or 540 μ m to render a sub-millimeter beam on the sample at an incident angle of ~ 25 deg. The beam flux was measured to be $\sim 10^{12}$ photons/s for a 260- μ m pinhole (Refs. 34–36) after the SPEAR 3 upgrade at SSRL in 2002. A photon energy of 12.0 keV ($\lambda = 0.1033$ nm) was chosen for most experiments to maximize the number of Bragg peaks in a selected 2θ window of (25–55 deg), and to be far enough in energy above the Fe-edge to minimize the background contribution due to Fe K-fluorescence from steel samples (Fe K-edge at 7.112 keV) (Ref. 47).

The SRXRD patterns were recorded downstream of the weld using a 50-mm-long 2048 element position sensitive Si photodiode array detector. This detector, together with the associated data acquisition system was manufactured by Princeton Instruments, was used to store and display the real-time X-ray diffraction data. The array was mounted on a dual-stage Peltier effect thermoelectric cooler, which in turn was water cooled, and was placed approximately 100 mm behind the weld to cover the 2θ range from 25 to 55 deg.

Once the diffraction patterns were acquired, the integrated intensity of each peak was then measured using a sum of one or more Gaussian peak profile fitting

functions (Ref. 48), and the results used to determine the semiquantitative volume fractions of the phases present as a function of welding time. This technique is summarized in detail in previous work (Refs. 49–52). In the Fe-based systems (steels, stainless steels) the 12-keV beam covers 2θ range that contains three ferrite peaks: bcc (110), bcc (200), and bcc (211); and three austenite peaks: fcc (111), fcc (200), and fcc (220). For titanium alloys (commercially pure and Ti-6Al-4V), this 2θ range encompasses three possible β -titanium peaks: bcc (110), bcc (200), and bcc (211); and 9 possible α -titanium (hcp) peaks (Ref. 49).

The SRXRD experiments were performed inside an environmentally controlled chamber as shown in Fig. 2, which is further confined inside a synchrotron radiation hutch. Prior to performing the experiment, the chamber was evacuated to 60 mTorr using a mechanical roughing pump and then backfilled with high-purity (99.999%) helium gas prior to running the experiment in order to deliver the X-ray beam with minimal attenuation to the sample and to prevent oxidation of the weld surface. Helium gas was flowed through the torch during welding to further prevent oxidation in the weld region and to cool the torch. An additional cross jet of helium gas was also directed at the X-ray beam impingement location to prevent metal vapors from depositing on the surface where X-ray diffraction was taking place. The chamber contains two 50-mm-diameter ports. The first port was sealed with a 0.125-mm-thick Mylar® window, which allowed the X-rays to enter the chamber. The second port was sealed with a KBr crystal and was used to video tape the weld using an infrared cam-

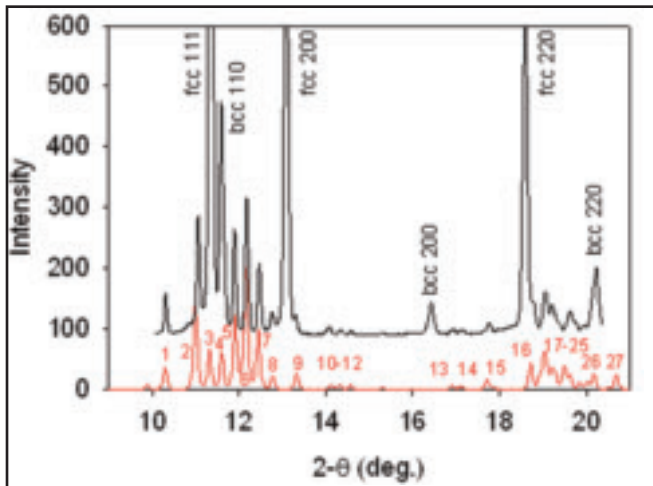


Fig. 5 — Room-temperature diffraction pattern of a duplex stainless steel alloy after heat treating to form sigma phase (black line) with the calculated diffraction pattern of the sigma phase (red line). Indexing numbers for the sigma phase correspond to the peaks summarized elsewhere (Ref. 59).

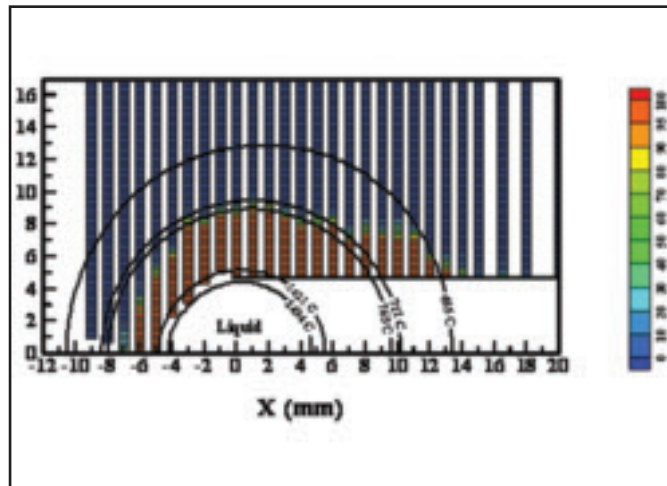


Fig. 6 — SRXRD semiquantitative map showing the volume fraction of austenite (red) in the 1045 steel HAZ. The scale indicates the amount of austenite (0–100%), and the calculated isotherms are shown for the liquidus, solidus, A3, A1, and bainite start temperatures.

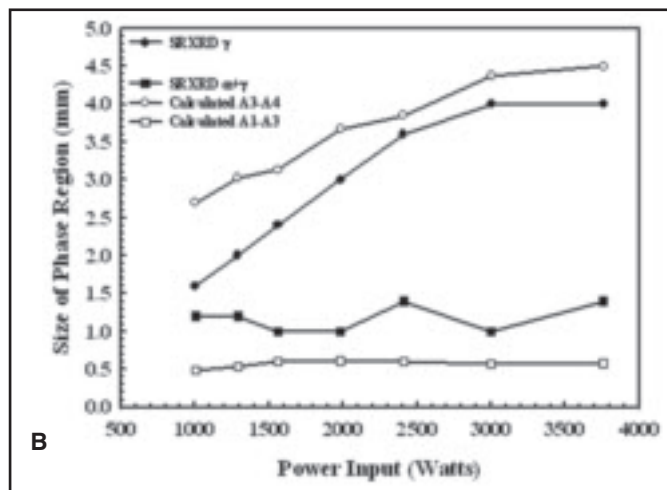
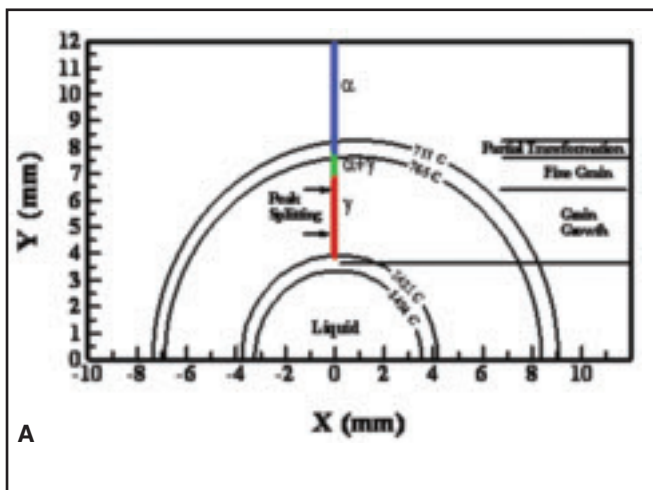


Fig. 7 — A — SRXRD experimental observations of the HAZ regions in 1045 steel compared to the calculated isotherms for a 1984 W GTA weld; and. B — SRXRD measured sizes of the HAZ phase regions, and calculated values based on the equilibrium transformation temperatures.

era (Inframetrics Inc. Model 600) with a 0.46-m focal length lens and a 40 × 25 mm field of view of the weld. This instrument provided real-time visual monitoring of the welding process.

The welding assembly was integrally mounted to a translation stage driven by a stepper motor with 10- μ m precision and placed inside the environmental chamber. Spatial mapping of the phases in the HAZ was performed using the translation stage to manipulate the weld (welding torch and workpiece) with respect to the fixed synchrotron X-ray beam in order to probe discrete regions around the weld. A typical SRXRD run consisted of gathering 40 diffraction patterns, each spaced 250 μ m apart (for a 260- μ m pinhole), along a pre-determined path to span a range of 10 mm through the HAZ in early experiments

(Refs. 8–10, 28–33). Later, after SSRL had gone through the Spear 3 upgrade in 2002, the higher beam flux allowed shorter integration times of 4 s/point, which allowed scans of 80 points that spanned 20 mm through the HAZ (Refs. 34–36).

A software package was developed on a personal computer using LabView software to control the position of the weld with respect to the X-ray beam, to control the bar rotational speed (welding speed), and to trigger the data acquisition system on a second computer. Each SRXRD data point was taken while the beam was at a fixed location with respect to the welding electrode, and X-ray data were collected (integrated) for times between 4 and 10 s, while the bar rotated under the torch at a constant speed. The resulting data were presented as a series of X-ray diffraction

patterns along a given X-ray scan direction perpendicular to and away from the centerline of the weld. After completing a run, the weld was allowed to cool to room temperature and the weld was repositioned to a new starting location with respect to the X-ray beam prior to taking the next series of SRXRD data. By repeating rows of X-ray diffraction data, equally spaced along the length of the weld, the phases in the entire HAZ region can be mapped.

Time Resolved X-Ray Diffraction (TRXRD)

The related TRXRD technique, illustrated in Fig. 1B, was developed to analyze transient arc welding conditions using rapid sampling X-ray diffraction for the observation of the phases that exist in the HAZ during rapid heating and cooling of

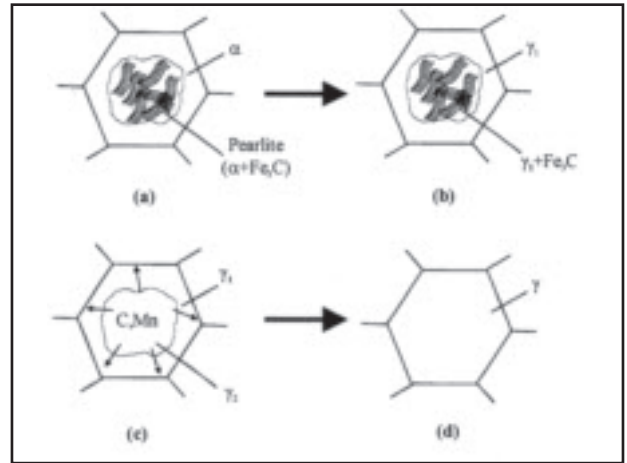
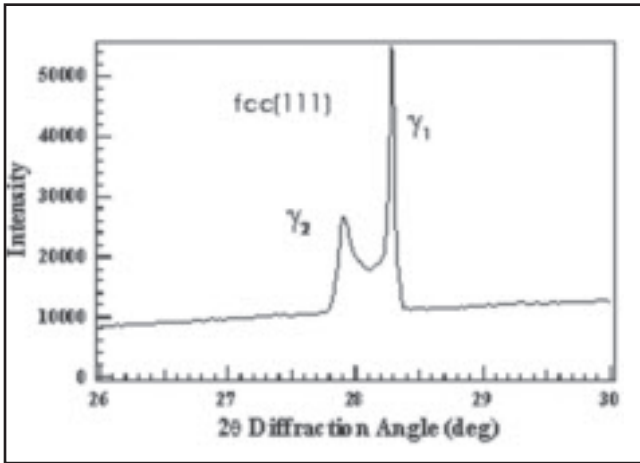


Fig. 8 — In-situ X-ray diffraction pattern showing splitting of the fcc(111) austenite peak (left). Schematic diagrams showing the progression of the $\alpha \rightarrow \gamma$ transformation during heating of 1045 steel (right).

GTA spot welds in real time. The transient spot welds heat and cool much more rapidly than steady-state welds and require different data acquisition methods to achieve the high temporal resolution (50 to 100 ms) necessary to monitor them.

The TRXRD technique developed at LLNL was designed for this rapid data acquisition, and consists of both X-ray diffraction and GTA spot welding components. TRXRD is performed in the same experimental chamber as the SRXRD experiment, but uses a stationary bar rather than a rotating bar. During the experiments, a highly focused synchrotron X-ray beam was directed at a single predetermined location on a 102-mm-diameter cylindrical bar while a GTA spot weld was being made. The location where the X-ray impinges can include the molten metal in the weld pool fusion zone (FZ), which allows solidification to be monitored, or in the weld HAZ, which allows high-temperature solid-state transformations to be monitored. Additional details about the specific TRXRD welding experiments are included in previous work, (Refs. 49–56),

and a summary of the experimental conditions and types of materials studied is shown in Table 1.

The TRXRD experiments were also performed using the same 31-pole wiggler beamline (10–2) at SSRL as the SRXRD experiments, and with the same photodiode X-ray detector. The synchrotron beam is spatially resolved by passing it through a tungsten pinhole with diameters up to 730 μm , to provide more signal than the SRXRD experiment, which is necessary to accommodate the shorter integration time per X-ray diffraction pattern. During each experiment, a stationary arc was maintained for a fixed amount of time, usually between 15 and 30 seconds to make the weld. After the arc was extinguished, the data acquisition continued taking data during cooling for a total of 60 s. These spot welds are approximately 10 mm in diameter, and the heating rates are calculated to be on the order of 100°C/s near the melting temperature of the alloy, while cooling rates are calculated to be on the order of 1000°C/s in the fusion zone (Ref. 25). These high cooling rates

achieved in the TRXRD experiment are approximately 10- \times faster than those achieved in the SRXRD experiment.

Controlled Heating and Cooling (CHC) Experiments

The SRXRD and TRXRD techniques described above are the only methods available for gathering real-time diffraction data on welds under real welding conditions. However, these techniques are difficult to perform in that they require welding equipment with sophisticated motion control and data acquisition systems to be set up on a synchrotron beam line. In addition, the weld temperatures, heating rates, and cooling rates, which are set by the weld parameters, are not directly controllable. Further, the rather large sample sizes are required to perform the experiments. Because of these constraints, a third synchrotron technique is employed that allows smaller samples to be used and controls the temperature during the experiment. This method uses direct resistance heating so that the sample can be

Table 1 — Overview of TRXRD Experimental Parameters

Materials System	Beam Energy (kV)	Beam Wavelength (nm)	Beam Size (μm)	Time Resolution (ms)
304L Stainless Steel	12.0	0.1033	730	50
	7.0	0.1771	730	50
Flux Cored Steel	12.0	0.1033	730	50
1005 C-Mn Steel	12.0	0.1033	730	50
	12.0	0.1033	260	100
1045 C-Mn Steel	12.0	0.1033	540	100
2205 Duplex Stainless Steel	12.0	0.1033	540	100
Ti-6Al-4V	12.0	0.1033	540	100

subjected to an arbitrary temperature profile. In addition, the X-ray diffraction patterns are measured with an areal detector for more accurate diffraction data. This technique has been used on many of the same materials as the SRXRD and TRXRD technique (Refs. 57–61), but also on new materials such as Cu-Au (Ref. 62), dual-phase sheet steels (Refs. 63, 64), and 9% Cr steels (Refs. 65–67). The drawbacks of this technique are that welding thermal cycles are only simulated and that melting/solidification phenomena cannot be observed. In addition, the present data collection rate is slow, so that rapid heating and cooling rates cannot be analyzed. Nevertheless, this method provides a very important complementary tool to SRXRD and TRXRD, and can be used to simulate heat treating as well as welding.

The *in-situ* CHC X-ray diffraction measurements were all performed on the UNICAT beam line BM-33-C at APS using a 30-keV X-ray beam from a ring current of 100 mA. This beam line was set up with a water-cooled Si (111) monochromator, and the beam was focused and sized to dimensions of 1 mm wide by 0.25 mm high using a dynamically bent Si crystal and collimator slits. The X-ray detector was manufactured by Roper Scientific (A99k401, RS/Photometrics). This X-ray detector uses 2×2 -in. array of 1024×1024 pixels spaced 60 microns apart to capture the diffraction patterns produced on a scintillating screen connected to the CCD array using a fiber-optic bundle. The overall CHC experimental setup is schematically illustrated in Fig. 3, where the X-ray beam is spatially resolved to a square shape using vertical and horizontal slits, the beam flux is measured using an ion gauge detector, and the diffracted beams are recorded using the areal detector placed downstream from the diffraction point. The sample is surrounded by an environmental chamber (not shown) that is first evacuated and then backfilled with high-purity helium to minimize oxidation of the sample during high temperature runs. The X-rays enter and exit the chamber through kapton ports on the front and back side of the chamber. The CHC coupons measure 100 mm long by 4.75 mm wide by 2 mm thick, and are clamped into a water-cooled-copper fixture that allows high currents to be passed through them as indicated in Fig. 3. This direct resistance heating of the coupon method can heat most samples at several 100°C/s , while water-cooled-grips allowed the sample to be rapidly cooled at similar rates however, the present data acquisition system limits the rates to approximately 20°C/s in order to correlate the temperature to the diffraction pattern with sufficient accuracy. The temperature of the sample is monitored and

recorded using type-S (Pt/Pt-10%Rh) thermocouples that are spot welded on the back side of the sample directly below the X-ray impingement point. A Eurotherm 818 temperature controller, a Eurotherm 425A power thyristor, and a Trindl RT300 transformer were used to control the AC current passing through the sample so that preprogrammed thermal cycles could be followed in a controlled manner. The heating power supply is capable of producing 300 A at 6 V and can heat steel samples up to temperatures as high as 1400°C .

While the sample is being heated, the X-ray beam impinges on the top surface of the sample at a 5-deg angle of incidence, and the diffracted beams are collected 330 mm downstream from the sample. The detector integrates the diffracted beams over a 1-s exposure time, and transfers these data to a computer to clear the detector for the next diffraction pattern. The transfer of data requires 2 s, thus it is possible to capture a complete diffraction pattern approximately every 3 s, but can be accelerated by about 1 s through a 2×2 binning of the pixels. An advantage of the 2-D detector is that statistically significant diffraction data can be collected for coarse-grained samples, which occurs by grain growth at elevated temperatures, as opposed to the narrow photodiode array detector used on the SRXRD and TRXRD experiments.

To calibrate the X-ray detector, the room-temperature lattice parameters of the base metal at room temperature are first measured using a conventional $\text{Cu K}\alpha$ X-ray diffraction system. A room-temperature pattern is then collected on this same sample using the CCD array detector on the synchrotron radiation beam line. Five points are then selected along each of the Debye arcs of the diffraction pattern. Finally, the sample-detector distance, the position of the center of the arcs on the detector, and the magnitude and orientation of the detector tilt are varied to minimize the difference between the d spacing at the selected points as calculated from these detector patterns and that calculated from the lattice parameters. Using this calibration, the Debye arcs are converted into a 1-D plot showing diffracted beam intensity vs. d-spacing using Fit-2-D

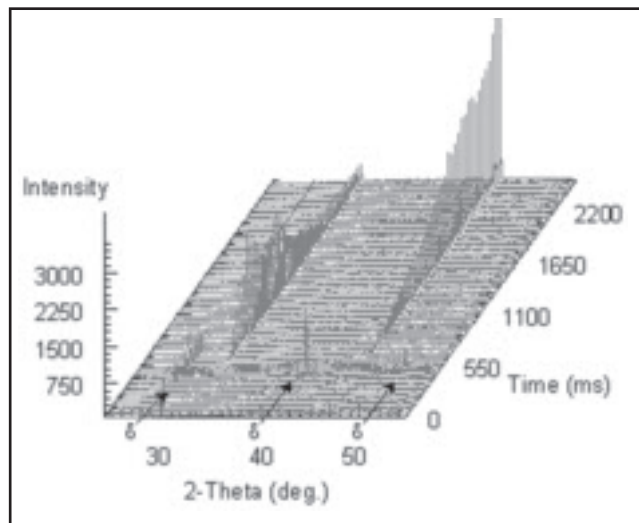


Fig. 9 — TRXRD patterns taken at 50-ms intervals during solidification of the AISI 304 stainless steel spot weld. The bcc peaks (denoted by \rightarrow) are the first to appear as solely the δ -phase for the first 500 ms. Coexistence of the δ and γ phases is observed during the next 200 ms followed by the appearance of only fcc peaks of the γ -phase to room temperature.

software (Refs. 68, 69). This software integrates the diffracted beam intensity for each arc over the entire 2-D areal array, creating a conventional intensity vs. 2θ diffraction pattern. The lattice spacing, FWHM value, and integrated intensity of each peak were determined using an automated curve-fitting routine developed in Igor Pro®, Version 4.0 (Ref. 48), and these data provide semiquantitative information about the amounts of phases present in each diffraction pattern.

Thermal-Fluids Modeling

The *in-situ* synchrotron welding experiments gather information about phases as a function of weld position (SRXRD) or weld time (TRXRD), but not as a function of weld temperature. Since the direct measurement of weld temperatures is very difficult to perform, due to the steep thermal gradients and intense conditions that exist around the plasma formed by the welding arc, weld thermal cycles are calculated using a well-tested coupled thermal fluids model. This model was developed by the Pennsylvania State University, and utilizes a 3-D numerical heat transfer and fluid flow code that was created specifically for fusion welds (Ref. 23). In this model, the equations of conservation of mass, momentum, and energy in three-dimensional form are discretized using the power law scheme and numerically solved by the SIMPLER algorithm (Ref. 70). The model solves the equations to determine the size, shape, and thermal profiles around the weld pool in three dimensions. After obtaining the steady-state temperature field, the thermal cycle at any

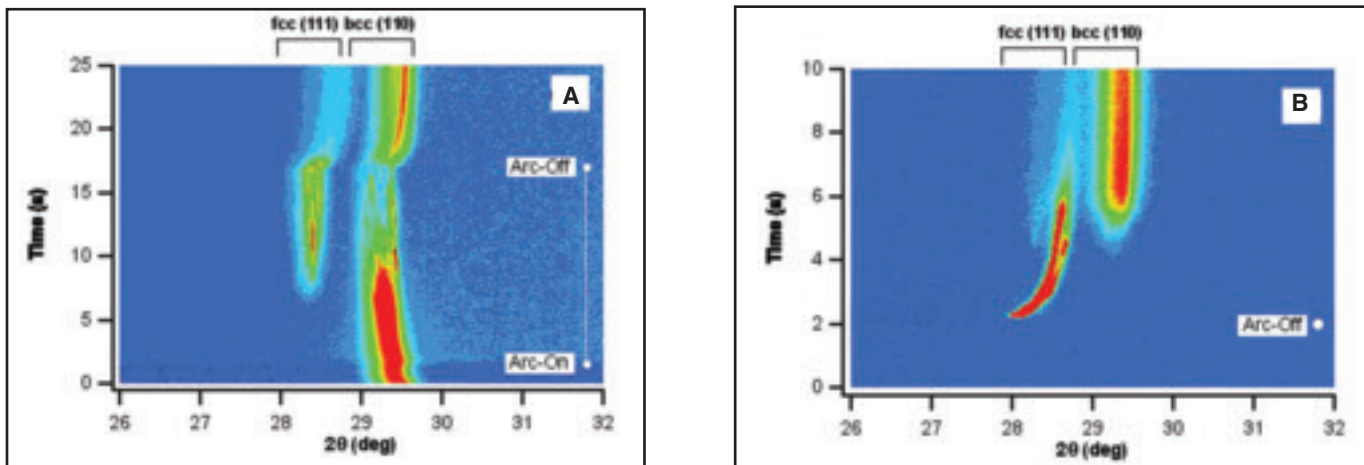


Fig. 10 — TRXRD diffraction data from — A — the HAZ region; and B — the FZ region of the high aluminum FCAW steel under rapid cooling spot weld conditions. The high-intensity diffraction data are represented by red, background intensity by blue. The arc-on and arc-off periods are shown. Data were recorded at 50-ms intervals.

given location (x,y,z) can be calculated using the following equation:

$$T(x,y,z,t_2) = \frac{T_s(\xi_2,y,z) - T_s(\xi_1,y,z)}{\xi_2 - \xi_1} V_s(t_2 - t_1) + T(x,y,z,t_1) \quad (1)$$

where $T(x,y,z,t_2)$ and $T(x,y,z,t_1)$ are the temperatures at times t_2 and t_1 , respectively, $T_s(\xi_2,y,z)$ and $T_s(\xi_1,y,z)$ are the steady-state temperatures at coordinates (ξ_2,y,z) and (ξ_1,y,z) , respectively, V_s is the welding speed; and $(\xi_2 - \xi_1)$ is the length welded in time $(t_2 - t_1)$.

In the SRXRD experiments, the thermal profile is determined in the steady-state weld for quasi-steady-state welding conditions represented by Equation 1; however, for transient welds, the calculations are much more complicated due to the fact that a quasi steady state is never reached and the weld pool size must be recalculated at each time step. This problem has been solved by the Pennsylvania State University group, and the model has been used to analyze the TRXRD experiments by calculating the transient thermal profiles as a function of time and position for the spot welding condition, where the size of the liquid pool is constantly changing (Ref. 25). From these results of the thermal calculations, the temperature profiles can be determined for any point relative to the weld center, and then further used as input to kinetic models for analyzing the synchrotron data. Applications of the heat and fluid flow model for the steady-state welds used for SRXRD are discussed in references (Refs. 32–37), while those for transient welds used for TRXRD are discussed in references (Refs. 49–51).

Computational Thermodynamics Modeling

The equilibrium phases of an allotropic metal or alloy change with temperature, and because of this, the HAZ of a weld will contain different subregions that are undergoing different phase transformations during welding. Low-carbon steels, for example, undergo two solid-state phase transformations before melting, resulting in a large austenite region surrounded by a thin layer of delta ferrite adjacent to the weld pool on one side and ferrite on the other (Refs. 31, 37). Although the different HAZ subregions are suspected to exist, the exact size of these zones relative to the weld pool is not known without direct first-hand observations or through verified phase transformation modeling.

Once the weld temperatures have been calculated, then the first step at estimating the location of the different HAZ subregions is to calculate the equilibrium phase transformation temperature isotherms in the HAZ. *Thermocalc*® (Ref. 71) was used to calculate the phase equilibria and transformation temperatures for all of the alloys investigated, and when coupled with the results of the thermal fluids model of weld temperatures, the equilibrium phase boundaries in the HAZ could be determined. Kinetic departures from equilibrium distort these equilibrium boundaries, extending the low-temperature phases into higher-temperature regions on heating, and the reverse on cooling (Refs. 28, 33, 35–37). By measuring the locations of the actual phase boundaries in the weld HAZ and comparing them to the calculated equilibrium boundaries, deviations between the two can be determined. The phase transformation kinetics can then be

extracted by these deviations from equilibrium.

Phase Transformation Modeling

Solid-state phase transformations in welds occur by different possible mechanisms. Some mechanisms, such as nucleation growth, involve diffusion (Refs. 11–13) and others, such as martensite, are based largely on displacement with little or no diffusion taking place (Refs. 11–13). In the majority of the SRXRD experiments, where heating and cooling rates were relatively low, the phase transformations take place by nucleation and growth mechanisms, and these were modeled by the Johnson-Mehl-Avrami (JMA) formulation. This approach can be represented by the following expression (Ref. 11):

$$f_c(t) = 1 - \exp\left\{-\left(kt\right)^n\right\} \quad (2)$$

where $f_c(t)$ is the extent of the transformation at a given time t , n is the JMA exponent, and k is a rate constant given as:

$$k = k_0 \exp\left(-\frac{Q}{RT}\right) \quad (3)$$

where k_0 is a pre-exponential constant, Q is the activation energy of the transformation including the driving forces for both nucleation and growth, R is the gas constant, and T is the absolute temperature in K. Equation 2 was modified to derive the JMA-based expression applicable phase transformations occurring in the two-phase region of the HAZ, and discretized so that it could be integrated over the non-isothermal weld profile (Ref. 37). This modeling approach was combined with

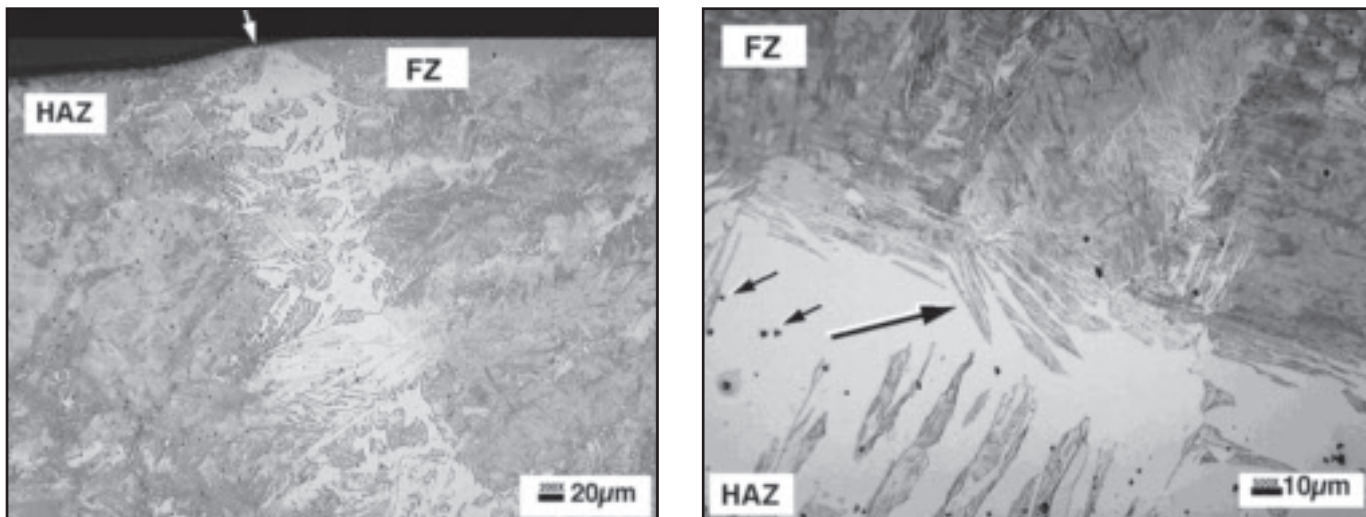


Fig. 11 — Micrographs of the HAZ-FZ boundary of the spot weld region in the FCAW alloy after TRXRD. The former δ ferrite (white etching phase) exists on both sides of the weld interface, before the change in solidification modes to austenite through the remainder of the fusion zone.

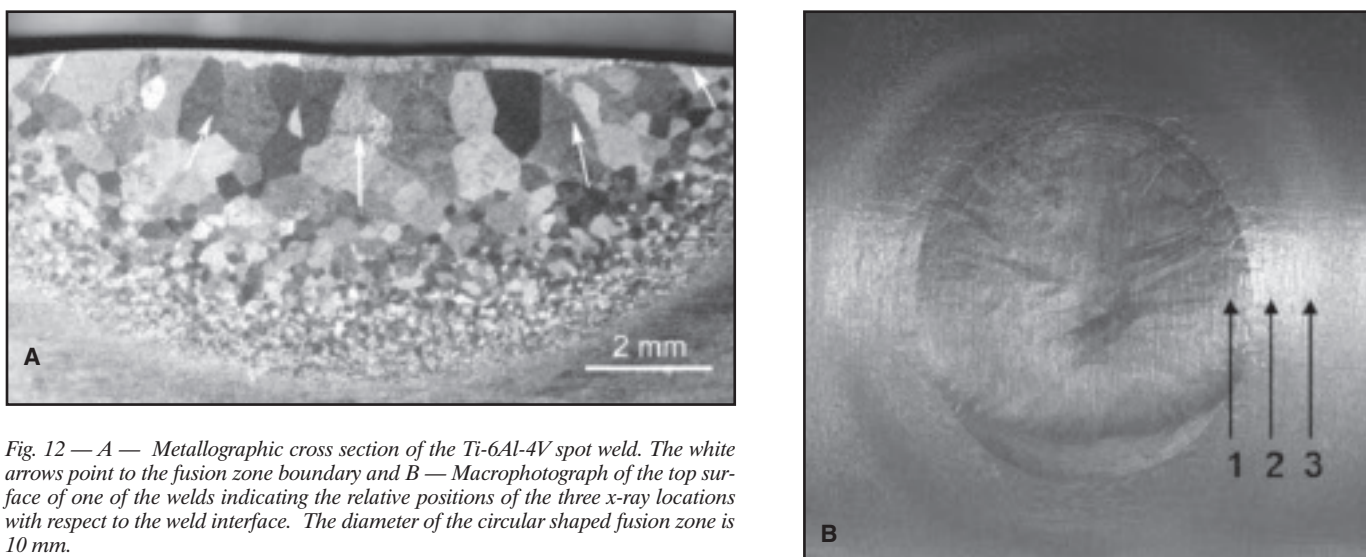


Fig. 12 — A — Metallographic cross section of the Ti-6Al-4V spot weld. The white arrows point to the fusion zone boundary and B — Macrophotograph of the top surface of one of the welds indicating the relative positions of the three x-ray locations with respect to the weld interface. The diameter of the circular shaped fusion zone is 10 mm.

the calculated thermal profiles and the SRXRD experimental data to determine the JMA parameters n and k_0 for the given value of Q using a graphical fitting routine applied to the SRXRD data (Refs. 37, 42, 43). Optimization of the JMA parameters from the limited amount of synchrotron data was later improved, using a parent centric recombination (PCX) based genetic algorithm (GA) to obtain optimized values of the JMA parameters (Ref. 38). The GA based determination of all three JMA equation parameters resulted in better agreement between the calculated and the experimentally determined phase fractions than was previously achieved, resulting in better predictability of the phase transformation rates (Ref. 38).

Additional models have been developed to analyze the synchrotron experimental results. These models include

phase transformation mechanisms in non-uniform starting microstructures (Ref. 44), nonequilibrium weld solidification (Refs. 53, 54), bainite and martensite formation during rapid weld cooling (Ref. 50), 3-D grain growth in weld HAZs using Monte-Carlo methods (Refs. 39, 40), and microstructure evolution using phase field modeling techniques (Refs. 45, 63, 64). Details of each of these techniques can be found in the cited references.

Selected Results and Discussion

The three synchrotron-based techniques, SRXRD, TRXRD, and CHC, have been used to investigate phase transformations in commercially available steels, stainless steels, titanium alloys, a flux cored arc welding (FCAW) consumable, and a gold-copper diffusion couple. Table 2 summa-

rizes the materials systems investigated and the different methods used on each. The results presented here highlight some of the findings for each technique, and demonstrate the capabilities that each possesses.

Spatially Resolved X-Ray Diffraction (SRXRD)

SRXRD X-Ray Diffraction Patterns and Analysis. During SRXRD, X-ray diffraction patterns are taken one at a time as the weld is moved relative to the synchrotron beam (Refs. 28, 31, 37). A typical sequence of diffraction patterns will contain 40–80 individual patterns, uniformly spaced across the HAZ of the weld. One such row of X-ray data is shown in Fig. 4 for 1005 steel, where there are three diffraction peaks for the bcc (ferrite) phase, and three diffraction peaks for the

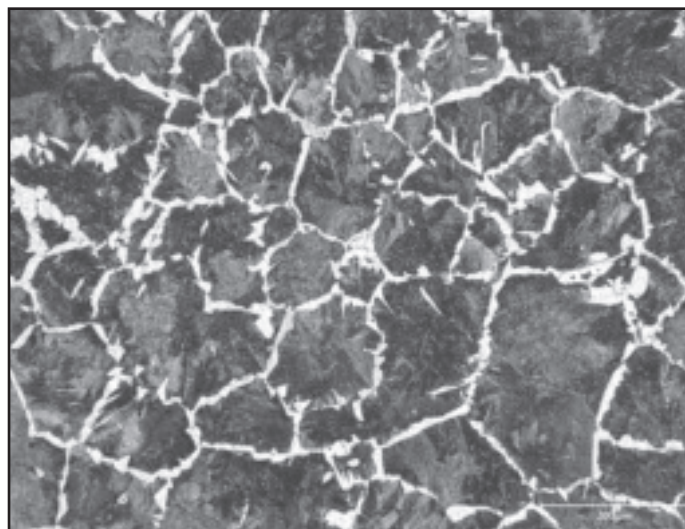
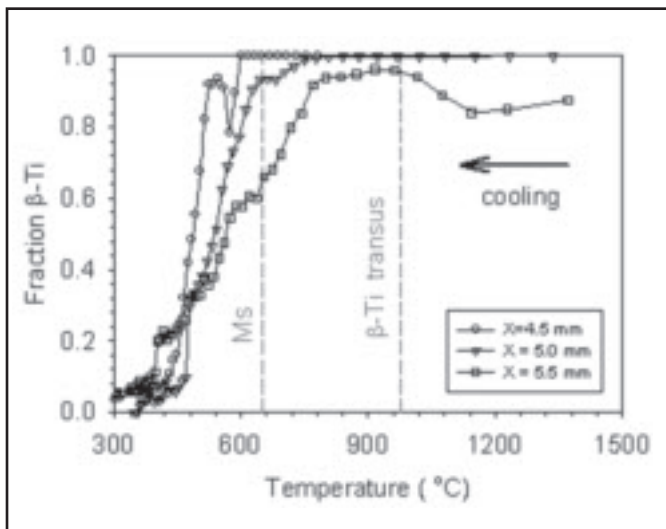


Fig. 13 — TRXRD results showing fraction β phase during the cooling cycle of the Ti-6Al-4V weld FZ and two HAZ locations plotted vs. the calculated weld temperature. The vertical dashed lines mark the calculated α/β transus, and the approximate Ms temperature for this alloy.

Fig. 14 — Base metal microstructure of the 1045 steel showing prior austenite grains and pearlite colonies inside the grains.

fcc (austenite) phase in the 2 θ diffraction window. These data show the progression of phases from liquid to δ -ferrite to austenite to α -ferrite as the HAZ is probed from high temperatures in the fusion zone toward the base metal in real time. The X-ray diffraction peaks from each diffraction pattern were then analyzed using peak area based methods specifically in the two phase regions to estimate the relative volume fractions of α and γ at each location in the HAZ (Ref. 37). The resulting data provide semiquantitative information about the relative amounts of each phase that exist at the given location in the HAZ.

The diffraction patterns shown in Fig. 4 for the C-Mn steel are rather straightforward since there are only two phases, and each phase has a cubic symmetry. However, in other systems such as duplex stainless steels, lower symmetry phase such as sigma phase can form with more

complicated diffraction patterns. Figure 5 shows one of these diffraction patterns where sigma phase coexists with both the fcc and bcc phases. Indexing the peaks of the sigma phase was performed with the aid of X-ray diffraction software (Ref. 72).

Once the X-ray diffraction patterns are indexed, additional analysis can be performed on them to determine the relative amounts of each phase in a given diffraction pattern, as detailed elsewhere (Ref. 37). In addition, the particular character of the diffraction peaks contains a wealth of information about the phases including annealing/recrystallization (Refs. 9, 28, 29, 31, 33, 51), oxide formation (Ref. 29), heterogenities in the starting microstructure (Refs. 35, 36, 57), and diffusion that occurs during the transformation (Refs. 60–62). These effects are beyond the scope of this paper, but additional information is provided in the cited references.

Phase Mapping of 1045 Steel Weld

The rows of diffraction patterns acquired by SRXRD can be taken at different locations along the length of the weld by repositioning the welding torch to different starting locations relative to the X-ray beam (Refs. 31, 33, 36, 37). By doing this repeatedly, the X-ray diffraction data can be acquired and analyzed to produce a semiquantitative map of the phases and phase fractions that exist in the HAZ during welding. Figure 6 shows one of these maps for a GTA weld in AISI 1045 steel at power of 2.4 kW and a travel speed of 0.6 mm/s (Ref. 37). More than 20 rows of data were required to complete the phase map, which contained more than 800 individual diffraction patterns in the weld HAZ.

The phases identified by SRXRD in Fig. 6 are then superimposed with the calculated temperature isotherms from the coupled thermal fluids weld model discussed previously. For the 1045 steel, the HAZ contains the base metal ferrite (α) and the high-temperature austenite (γ) and a transition region where both phases coexist in-between. The locations of the α and γ phases are plotted with 250 μ m precision perpendicular to the welding direction and 500 μ m parallel to the welding direction. In this map, the shading indicates the γ fraction. The map shows a variation in γ from 0 to 100% over a narrow region approximately 1.0 to 1.6 mm wide that borders the rather large γ phase field that surrounds the weld pool.

The HAZ map shows that the γ phase field is wider on the trailing side of the weld than on the front side. It is also ap-

Table 2 — Summary of the Synchrotron Techniques Used to Investigate Different Materials, and Phase Transformation Modeling Papers Based on or Verified by the Experimental Results^(a)

	SRXRD	TRXRD	CHC	Phase Transformation Modeling
1005 Steel	31	55	57	37, 38, 41, 42, 43, 45
1045 Steel	34, 35, 36	50		
CP Titanium	8, 9, 10, 28, 29, 30			39, 40
Ti-6Al-4V	32	49	60, 61	
304 SS	8	52		
2205 Duplex SS	33	51	58, 59	44
FCAW		53, 54		
Cu-Au			62	
Dual-phase 600 steel			63, 64	63, 64
9% Cr Steel			65, 66, 67	

(a) The numbers in the table refer to the references cited in this paper.

parent that the completion of the $\alpha \rightarrow \gamma$ phase transformation is shifted to higher temperatures on heating, while the $\gamma \rightarrow \alpha$ phase transformation is shifted to lower temperatures on cooling relative to the calculated A3 temperature.

Analysis shows that superheating up to 250°C above the A3 temperature is required to completely transform the microstructure to γ on heating under these welding conditions, and that substantial undercooling below the A3 is required to initiate the transformation to α on cooling (Ref. 36). The lag required to complete the transformation to γ on heating is displaced further from the A3 isotherm at locations closer to the weld centerline where the heating rates are the highest, showing that the amount of superheating required for the $\alpha \rightarrow \gamma$ transformation varies with the location and thus the heating rate. Furthermore, during cooling, the region closest to the fusion zone requires the highest undercooling prior to measurable amounts of austenite transformation. The significant undercooling below the A3 isotherm correlates with the formation of bainite, which results from the larger austenite grain sizes and higher cooling rates in this region of the weld (Ref. 37).

Effect of Weld Heat Input on HAZ Width

In addition to mapping weld phases at a given heat input, SRXRD can also be used to determine the maximum width of the different HAZ phase regions as a function of welding heat input. Variations in the size of the observed γ phase field in steels occur as a result of changes in the weld heat input, and these effects were studied in the 1045 steel using SRXRD for weld power levels between 1 and 4 kW and a travel speed of 0.6 mm/s (Ref. 35). The locations of the γ , $\alpha + \gamma$, and α phase regions measured in the SRXRD scan made at a weld input power of 1984 W are shown Fig. 7A as an example, indicating that the high-temperature austenite field is nearly 3 mm wide under these conditions. The calculated isotherms for the liquidus, solidus, A3, and A1 temperatures, and the locations of the HAZ microstructural features observed in the postweld metallography are also shown (Ref. 35).

The widths of the γ and $\alpha + \gamma$ phase regions as measured by SRXRD are plotted in Fig. 7B (solid symbols) for the 1–4 kW range of weld powers. The austenite field is shown to increase from 1.5 to 4.0 mm over this range, while the mixed austenite plus ferrite region remains relatively constant between 1 and 1.5 mm. These values are compared with the calculated sizes of these phase regions based on thermodynamic considerations (open symbols). The variations between the calculated and ex-

perimental sizes of the γ -phase region differ over the range of powers investigated, and the differences are largest at the lower powers where the temperature gradients are highest. The size of the $\alpha + \gamma$ phase region remains fairly constant over the range of powers, but the measured width of the $\alpha + \gamma$ phase region is always larger than the calculated value due to the kinetics of the phase transformation that require higher than equilibrium temperatures to complete the transformation on heating.

Homogenization of Heterogeneous Starting Microstructures

In the 1045 steel welds, austenite was observed to form inhomogeneously on heating, which resulted in the creation of two distinct sets of X-ray diffraction peaks for all of the heat inputs investigated. The splitting of the austenite peaks occurs over a finite region of the austenite phase field as indicated by the two arrows in Fig. 7A for the 1984-W weld. Additional results are presented in Refs. 34, 35. When the austenite peaks split, a higher d-spacing (lower 2θ) austenite, γ_2 , begins to form on the initial austenite, γ_1 . Figure 8 shows one of these split peaks for the fcc(111) reflection at a location 5.2 mm from the weld centerline. The splitting is first observed near a calculated temperature of 884°C, which is approximately 100°C above the A3 temperature. The larger γ_2 lattice parameter is the result of higher concentrations of C and Mn in it. The primary source of these alloying elements is the undissolved cementite laths, which begin to dissolve into the austenite at elevated temperatures. Initially, the split between the γ_1 and γ_2 peaks is rather small, since γ_2 first begins to form from the γ_1 located within the pearlite colonies. With increasing temperatures, the amount of splitting increases as both C and Mn diffuse from the cementite into the γ_2 constituent. The amount of peak splitting reaches a maximum as the temperature approached 1250°C, which is assumed to correspond to the completion of cementite dissolution (Refs. 34, 35).

The peak splitting behavior and its disappearance at higher temperatures provides evidence of both the mechanism for the transformation of the base metal mi-

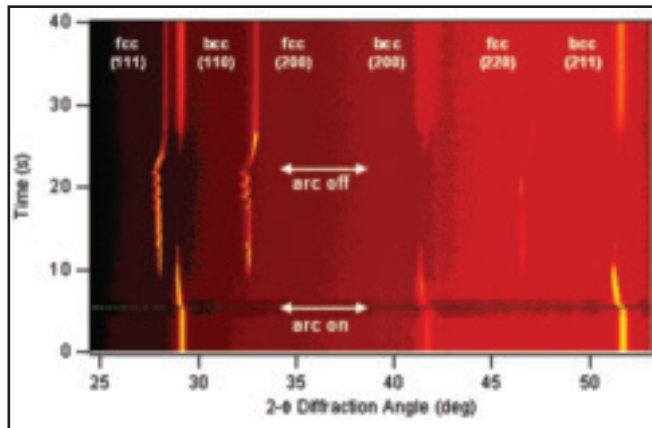


Fig. 15 — TRXRD results showing the changes in the diffraction peak locations as a function of welding time for the 1045 steel HAZ-+

crostructure and the homogenization of the resulting austenite phase during welding. This austenitization mechanism is schematically shown in Fig. 8B, where in the initial stages, ferrite in the pearlite colonies and allotriomorphic ferrite regions that surround them in the base metal (a) is transformed into austenite, γ_1 , (b). Because of the rapid heating cycles experienced in the weld HAZ, the cementite laths that are originally a part of the pearlite colonies do not completely dissolve before the ferrite in the microstructure is completely consumed above the A3 temperature. These cementite laths begin to dissolve with continued heating, introducing C and Mn into the austenite and causing a second, more highly alloyed austenite constituent, γ_2 , to appear (c). As the heating continues, these alloying elements, which originated in the cementite laths, continue to diffuse into the less highly alloyed γ_1 constituent. At temperatures of approximately 1300°C and above, the chemical composition of the austenite becomes homogenized into one austenite phase, γ , (d).

Time Resolved X-Ray Diffraction (TRXRD)

Transient arc welds are commonly encountered in tack welding, stationary spot welds, and solidifying weld craters, and they behave differently than moving welds because the temperature profiles never reach a steady state. Because of their transient nature, the heating and cooling rates for these welds are often much higher than those observed in moving welds, potentially leading to the formation of non-equilibrium phases not observed under slower cooling conditions. One attribute of TRXRD is that it can reveal insight about the microstructural evolution, starting from solidification all the way to room temperature, and can be done with time resolutions on a scale fast enough to

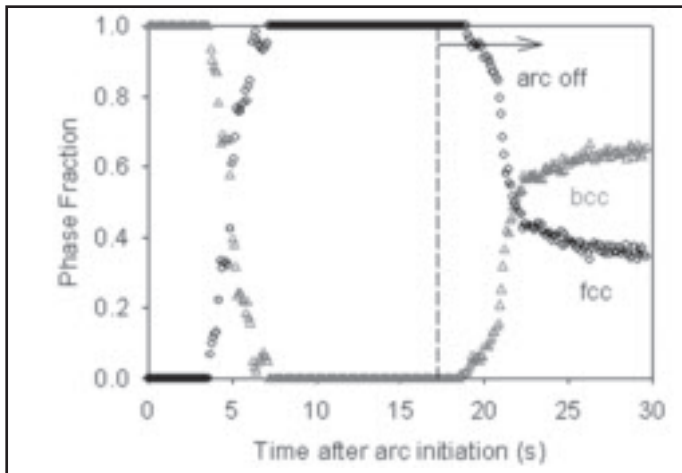


Fig. 16 — Analysis of the TRXRD diffraction patterns shown in Fig. 15 illustrating the relative fraction of the bcc and fcc phases as a function of arc welding time in 1045 steel.

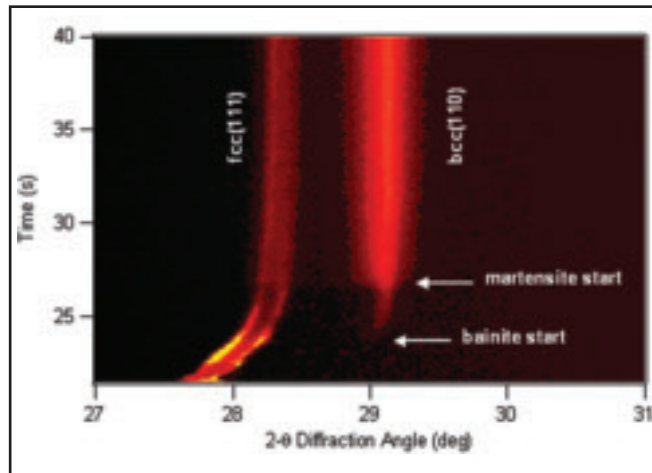


Fig. 17 — TRXRD results showing the fcc(111) and bcc(110) diffraction peaks during weld cooling. Martensite formation is accompanied by a rapid increase in peak width. Splitting of the austenite peaks continues during cooling due to insufficient time for homogenization of austenite in the TRXRD spot weld.

capture the formation of nonequilibrium phases. In the sections below, several results are presented for observations of the solidification mode and solid-state phase transformations that highlight TRXRD observations of nonequilibrium phase formation.

Primary Solidification Mode in 304 Stainless Steel

TRXRD was used to observe the dominant mode of solidification in an austenitic 304 stainless steel and the ensuing microstructural evolution during cooling (Ref. 52). Particular effort was made to verify the formation of δ -ferrite as the primary solidification phase from the melt anticipated based on previous work (Ref. 73), and to monitor the $\delta \rightarrow \gamma$ phase transformation during rapid cooling. In the TRXRD experiment, the X-ray beam was positioned at a distance of 2 mm from the electrode, which was well within the fusion zone of the spot weld, allowing solidification to be monitored. The results from one experiment are shown in Fig. 9, where liquid formed quickly after the arc was struck, as indicated by an initial period of featureless diffraction (Ref. 52). The arc was extinguished and as the weld pool solidified, bcc δ -ferrite diffraction peaks were observed first. All three bcc peaks exist by themselves for a period of 500 ms (10 frames), although not all three peaks were observed together in any given frame due to the large grain size and grain rotation. Transformation of δ to γ began in the next frame with both δ and γ diffraction peaks appearing together. The δ peaks coexisted with γ peaks for 200 ms (four frames) during the transformation. Upon

further cooling, only the γ peaks persisted in the remaining frames down to room temperature. The most significant finding of these TRXRD results is that δ -ferrite was verified as the first phase to solidify from the 304 stainless steel liquid weld pool. Although δ -ferrite solidification has been speculated, these results represent the first time that it has been observed.

Nonequilibrium Solidification of a FCAW Consumable

The TRXRD technique was used to determine the primary mode of solidification of a Fe-C-Al-Mn steel weld (Fe 0.23C-0.5Mn-1.7Al 0.28Si-0.02Ni-0.003Ti-0.006O-0.06 Nwt%). The steel was produced from a self-shielded flux cored arc welding (FCAW) electrode as a thick cladding over a solid steel bar (Refs. 53, 54). The high aluminum content of the FCAW electrode is intentionally added to deoxidize and denitride the weld because the flux cored welding process does not use gaseous shielding; however, residual aluminum is left in the weld deposit. Under conventional welding conditions, the added aluminum promotes formation of δ -ferrite during solidification. The aluminum also stabilizes the δ -ferrite at lower temperatures and prevents formation of 100% austenite during cooling. A small amount of austenite forms in the interdendritic regions, and decomposes to either bainite or pearlite depending upon the cooling rate. Thus, under low cooling rate conditions, the fusion zone inherits the high-temperature columnar δ -ferrite microstructure that is present at room temperature and can adversely affect the mechanical properties of the weld.

Under rapid weld cooling of this same alloy, the final weld microstructure contains allotriomorphic ferrite, bainite, and martensite, similar to that expected to form from an austenitic microstructure (Refs. 53, 54). The absence of columnar δ -ferrite in these rapidly cooled welds could be explained theoretically using two paths of phase evolution. In the first path, the liquid transforms to 100% δ -ferrite before transforming to 100% austenite by a massive transformation. The massive austenite then transforms to a mixture of allotriomorphic ferrite, bainite, and martensite during subsequent cooling. In this second path, the liquid transforms to 100% austenite by non-equilibrium solidification and then transforms to a mixture of allotriomorphic ferrite, bainite and martensite during subsequent cooling. TRXRD was used to determine the correct microstructure evolution path.

Figure 10A shows the TRXRD results from the following: 1) the HAZ, and 2) FZ regions of the FCAW steel during welding (Refs. 53, 54). The TRXRD measurements in the HAZ provide evidence for the persistence of δ ferrite in the HAZ. In a second experiment, FCAW solidification was observed as shown in Fig. 10B. Here it is clear that the liquid (no diffraction peaks) continued to exist as the only phase for 0.2 s after the arc was extinguished. Austenite then formed as the first solid phase as indicated by the appearance of the fcc (111) peak. As cooling continued, the austenite peaks shifted toward higher 2θ values, indicating a decrease in the lattice spacing due to a drop in temperature. Approximately 3 s after the onset of solidification, ferrite began to form from the austenite, as indicated by the appearance of the

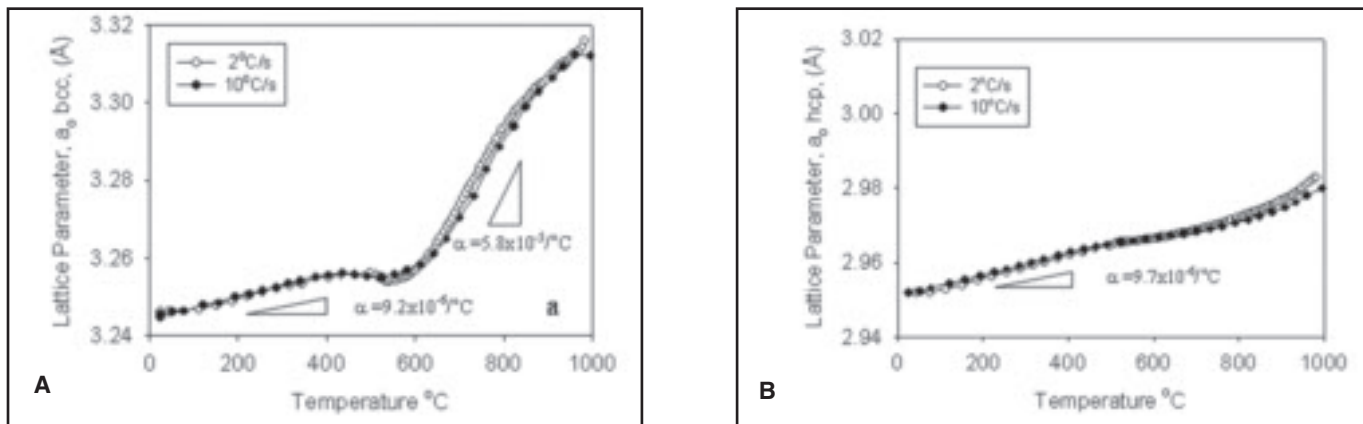


Fig. 18 — Lattice parameters alpha and beta phases in Ti-6Al-4V measured by in-situ X-ray diffraction as a function of temperature. A — The bcc (beta) phase; B — the hcp (alpha) phase during heating at two different rates. The indicated coefficients of thermal expansion, α , were calculated from the slopes of the curves.

bcc (110) peak. Upon further cooling, the ferrite peaks also shifted toward higher 2θ values as the temperature approached ambient conditions.

Primary austenite solidification for this high-aluminum FCAW alloy was verified through repeated experiments, in contrast to primary delta-ferrite solidification as predicted by thermodynamic calculations (Refs. 53, 54). The postweld microstructure of the FCA weld is shown in Fig. 11. The white etching region near the weld interface (marked by arrow) is identified as the δ -ferrite that formed in the HAZ at high temperature, which is further confirmation that the equilibrium ferrite mode of solidification can be replaced by non-equilibrium austenite even when the fusion boundary is surrounded by ferrite if the cooling rates are fast enough.

Martensite Formation during Cooling of Ti-6Al-4V

During solidification of Ti-6Al-4V, the fusion zone contains large columnar grains that solidify initially as β , and subsequently undergo a near complete transition to finely dispersed α or α' phase (Ref. 49). Figure 12A shows the microstructure of a Ti-6-4 spot weld, where the HAZ/FZ boundary is revealed as a dark etching line that runs through the columnar grains, and is identified by the arrows. Large grains exist on both sides of the weld interface, indicating significant grain growth in the HAZ, which is important to note since grain size can influence the phase transformation kinetics. The TRXRD technique was used to evaluate the phase transformation kinetics of this alloy by observing the welds at the three different locations, indicated in Fig. 12B, where position 1 indicates the location in the FZ, and positions 2 and 3 indicate locations in the HAZ.

Analysis of the three TRXRD measurements was performed and the results

are compiled in Fig. 13, which shows the fraction β during weld cooling of the Ti-6Al-4V in the FZ and two HAZ locations (Ref. 49). This figure shows that the $\beta \rightarrow \alpha$ transformation begins at a different temperature for each point relative to the center of the weld. At the two HAZ locations ($x = 5.0$, $x = 5.5$ mm), the $\beta \rightarrow \alpha$ begins at nearly the same time and at temperatures between the beta transus and martensite start temperatures, where it is clear that there is $\sim 100^\circ\text{C}$ of undercooling below the β transus before the transformation begins. For the measurements made in the weld FZ ($x = 4.5$ mm), the transformation is first observed at 600°C , which corresponds to much larger undercoolings, approximately 375°C below the β transus, which is also below the calculated M_s temperature for this alloy (Ref. 49). Once initiated, the $\beta \rightarrow \alpha$ transformation in the FZ occurs rapidly and nearly completely to α' martensite in less than 2 s over a temperature range of approximately 200°C .

Bainite and Martensite Formation in Carbon Steels

The carbon content and cooling rate both have a profound influence on the microstructures that develop during welding of steels. This effect was studied using TRXRD to compare microstructural evolution in spot welds for 1045 and 1005 steels, having 0.45 and 0.05 wt-% carbon, respectively. The results showed different behaviors for the two steels in that a combination of bainite (nonlamellar ferrite plus Fe_3C) and martensite (interstitial carbon) was observed forming in the microstructure of the 1045 steel (Ref. 50), but these phases were not observed during welding of the 1005 steel under similar welding conditions (Ref. 55).

Figure 14 shows the base metal microstructure of the 1045 C-Mn steel. Ferrite outlines the prior austenite grain

boundaries while pearlitic colonies dominate the microstructure inside these grains. In the TRXRD experiments, the X-ray beam was placed at a fixed location in the HAZ during heating and cooling to observe the phase transformations, and the resulting data from one experiment are shown in Fig. 15 (Ref. 50). In this figure the baseline diffraction data correspond to the three diffraction peaks of the bcc ferrite phase. After the arc is struck, these three peaks rapidly shift to lower 2θ values as the crystal lattice of the steel expands during heating. With continued heating, three new peaks appear, corresponding to the fcc austenite phase. All six peaks coexist for several seconds before the bcc peaks began to fade in intensity, leaving only the fcc diffraction peaks. The fcc peaks remained stable until the arc was extinguished at 17 s after arc initiation. The fcc peaks then rapidly shift to higher 2θ values as the lattice contracts with cooling. With an additional 1.5 s of cooling, the bcc peaks reappear, and increase in intensity as the weld cools. Analysis of these results is shown in Fig. 16 where relative fractions of the bcc and fcc phases present throughout the weld are plotted (Ref. 50).

A closer look at the diffraction patterns shows that the bcc (110) peak has a sudden increase in width at $t = 26$ s on cooling. Figure 17 shows this peak broadening where the wider bcc(110) peak exists throughout the remainder of the weld and increases in intensity as the weld cools. The sudden increase in the bcc(110) peak width during rapid cooling was not observed in similar experiments performed on the 1005 C-Mn steel (Ref. 55). The increase in peak width in the 1045 C-Mn steel is a consequence of its higher carbon content and the corresponding formation of body centered tetragonal (bct) martensite. The formation of martensite induces significant levels of strain and causes changes in the lattice parameters including the observed peak

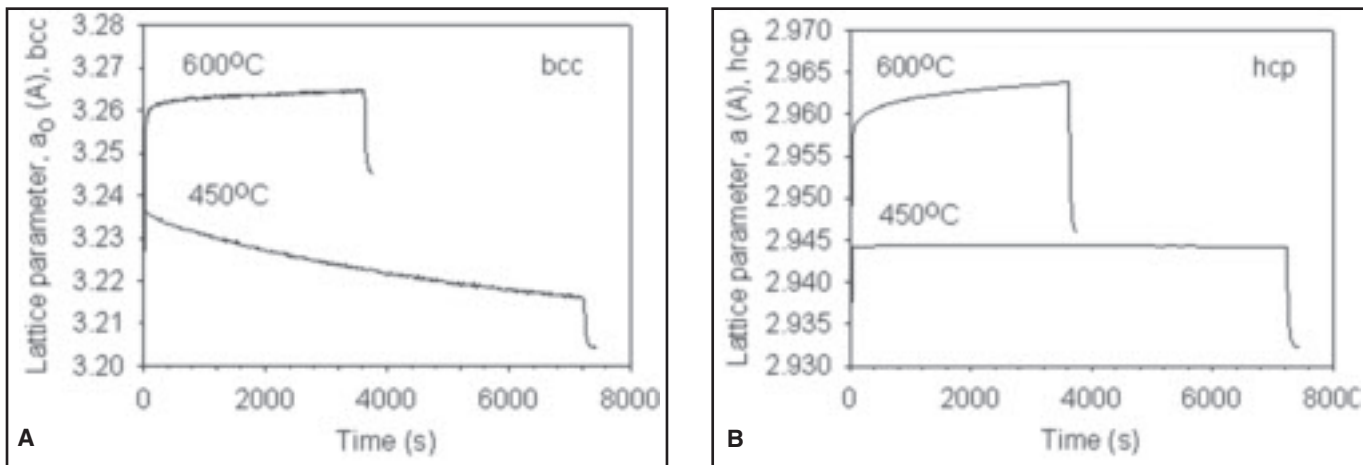


Fig. 19—In-situ lattice parameters measured by CHC for Ti-6Al-4V as a function of isothermal hold time at 450° and 600°C for the following: A—the β phase; B—the α phase.

broadening. A simultaneous broadening of the austenite peaks was observed, which is consistent with the strain induced in it by the surrounding martensite. These results demonstrate both the differences in the phase transformation behavior of low and medium carbon steels, and how *in-situ* X-ray diffraction can be used to provide real-time observations of important phase transformations during the welding of steels.

Controlled Heating and Cooling (CHC)

The CHC method allows samples to be subjected to arbitrary thermal profiles to heat and cool them to any temperature up to their melting point. Because of its simplicity, the CHC method can be used to both simulate welding and perform heat treating of any metal that can be resistively heated. The heating method is similar to that of a Gleeble experimental setup, while at the same time providing *in-situ* X-ray diffraction of the phases that are forming. A number of different materials systems have been investigated using this technique (Refs. 57–67), and here we present two examples of the types of data that can be obtained.

Stress Relieving and Phase Transformations in Ti-6Al-4V

Two different phases coexist in Ti-6Al-4V at room temperature: the low temperature alpha phase, which has a hexagonal close-packed structure, and the high-temperature beta phase which has a body-centered cubic structure. At elevated temperatures during heat treating or welding, the alpha phase transforms to beta. During cooling the reverse transformation occurs, which creates stress gradients on the microstructural scale due to different thermal contraction rates of the two phases (Ref. 61). Through *in-situ* diffraction a

surprising and unexplained dip in the beta lattice parameter occurred, as indicated in Fig. 18 (Ref. 61). The CHC method was used to examine the details of this lattice contraction dip on heating in more detail, and was particularly useful in that it can follow the individual lattice parameter developments of both the alpha and beta phases simultaneously (Ref. 61).

The CHC experiment was performed on Ti-6Al-4V alloy specimens that were machined from mill-annealed bar stock, which contained a small amount of beta phase distributed among and around the elongated grains of the alpha phase (Ref. 60, 61). Microprobe analysis was used to determine the compositions and amounts of the two phases, indicating an initial distribution of 87.9% alpha and 12.1% beta. The CHC diffraction measurements were carried out at the UNICAT beam line BM-33-C of the Advanced Photon Source, where 30 keV X-rays were passed through a silicon monochromator and focused to a beam 1 mm by 0.25 mm. Diffracted X-rays were collected with a CCD detector with the samples held at temperatures ranging from 400° to 650°C. Lattice expansion data were extracted from shifts in the Bragg peak positions as a function of time during ramping to and holding at the predetermined temperature (Ref. 60).

Figure 19 shows plots of the lattice parameters of both phases, and shows that they increase with temperature due to conventional thermal expansion during the first seconds of the experiment. Once the isothermal temperature is reached, the lattice parameter of the beta phase alone steadily decreased over a period of hours when held at 450°C (Ref. 60). In contrast, when the temperature was held at 600°C, the lattice parameter for the beta phase increased slowly over a comparable duration. The alpha phase, on the other hand, exhibited constant lattice parameter

at 450°C and a slower increase at 600°C as shown in Fig. 19B. Other temperatures were investigated (Ref. 60), and the beta phase lattice parameter exhibited its largest contraction at 450°C before expanding again with temperature, while the alpha phase showed no such dip within experimental error (Ref. 60). Further results show that the time-dependent change in beta lattice parameter at temperatures below 550°C occurs mainly from relaxation of preexisting stress in the starting microstructure. Above 550°C, the change in the lattice parameter of beta is caused mainly by the alpha to beta phase change and the subsequent redistribution of vanadium from alpha to beta (Ref. 60).

Sigma Phase Formation in 2205 Duplex Stainless Steel

Duplex stainless steel (DSS) alloys are often processed to have nearly equal amounts of ferrite and austenite in the microstructure, which provides them with a desirable combination of strength, toughness, and corrosion resistance. However, when exposed to elevated temperatures between approximately 600° and 1000°C for sustained periods of time, several undesirable intermetallic phases can form (Refs. 58, 59). The σ phase is the most prominent of these intermetallic phases, and once formed, sigma is known to adversely affect the mechanical properties and corrosion resistance of DSS alloys. Figure 20 shows the microstructure of a DSS after elevated temperature heat treating at 850°C where abundant σ phase has formed. Here, the CHC technique was used to observe the formation of σ phase at different temperatures to determine the kinetics of its formation (Ref. 58), and to observe the dissolution of sigma at temperatures approaching 1000°C (Ref. 59).

An *in-situ* diffraction pattern taken of

a DSS alloy after heat treating to form sigma phase was shown in Fig. 5 to illustrate the complex diffraction nature of the sigma phase. By taking diffraction patterns such as these repeatedly over the course of an elevated temperature cycle, the sigma phase formation can be observed and measured in real time. Figure 21 shows the results of the CHC X-ray diffraction data plotted for the initial 3700 s of a hold at 850°C. In this figure, the series of diffraction patterns are plotted with time along the y-axis, d-spacing along the X-axis, and the intensities of the diffraction peaks represented by different colors. The heating initiates at $t = 0$ s, and immediately all of the fcc and bcc diffraction peaks of the room-temperature microstructure shift to higher d-spacings due to the thermal expansion effect while the sample is being heated to 850°C. During holding, the intensity of the bcc peaks began to decrease while the intensity of the fcc peaks increase. At $t = 81$ s, the first sigma peak (411) appears, 40 s into the isothermal hold. With increased holding time, this peak intensifies and additional sigma peaks develop. Analysis shows that the sigma phase reached a maximum of 13.4% before beginning a thermal ramp to 1000°C at $t = 1850$ s. As the temperature ramps up the amount of sigma decreases, eventually reaching 0% at a temperature of 985°C. Sigma does not reappear again until the sample has been cooled back down and held at 850°C (Ref. 59).

A summary of the measured fractions of sigma, ferrite, and austenite is shown in Fig. 22, which also includes the temperature profile for this experiment. It is clear that sigma forms in increasing amounts until the temperature begins to ramp from 850° to 1000°C, reaching 0% at 985°C. This observed dissolution temperature for sigma is more than 100°C higher than predicted by thermodynamics (Ref. 59), and again is a measure of the kinetics of the phase transformation under a constant heating rate such as that produced during welding. The synchrotron data was modeled using a modified Johnson-Mehl-Avrami analysis (Refs. 58, 59), which provided kinetic data for sigma phase formation, and can be used to predict sigma phase formation under other welding and heat treating conditions.

Future Work and New Possibilities

SRXRD and TRXRD have proven to be unique and powerful tools to study microstructural evolution during welding, providing welding researchers with new capabilities. When combined with additional experiments such as *in-situ* CHC diffraction, and modeling of the results, a

deeper understanding of the kinetics of phase transformations that occur during welding can be realized. As synchrotron-based investigations of welds gain more widespread use, they will provide the welding research community with the ability to quantitatively describe the kinetics of more complex phase transformations and improve the knowledge base for understanding welding in ways not possible using conventional methods.

Looking into the future, these powerful synchrotron-based tools can be expanded to other areas of interest and different materials systems; however, the current SRXRD and TRXRD experimental setups are limited by two factors. First, the large size of the samples currently used for these experiments preclude investigations of potentially interesting materials systems of less common materials. Changes will be required to the experimental setup to allow different sample geometries, and thus a wider range of materials systems to be studied. This can easily be done for the TRXRD experiment where relatively small sample volumes are required. However, for the SRXRD experiment that requires a steady-state weld, different techniques will need to be developed. One method to reduce the SRXRD sample size is to acquire the data more rapidly. If the data can be acquired in a fraction of a second per data point, rather than the current 4–10 s per data point, then the total welding time, and thus the sample size, can be reduced accordingly. Methods where an entire row of data points can be acquired at one time using imaging plates (Ref. 74) could be developed further using digital imaging plate technology for example, which could rapidly speed up the SRXRD weld mapping process.

A second limiting factor to the existing setup is the speed and resolution of the X-ray detectors, which becomes even more important as higher data-sampling rates are desired. Even though the current silicon photodiode array detector used for SRXRD and TRXRD can capture X-ray diffraction patterns on the order of milliseconds, its linear geometry is only able to detect a small slice of the Debye circle, thus making the results susceptible to the

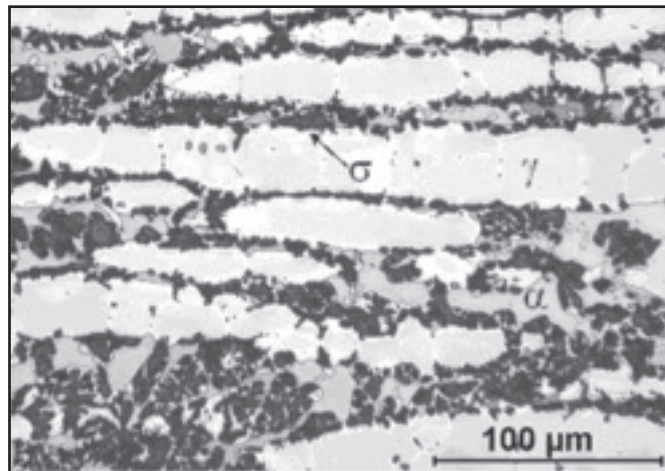


Fig. 20 — Optical micrograph showing the microstructure of the sample after the heat treating cycle. Ferrite, α , etches blue/purple in color, austenite, β , etches tan/white in color, and σ phase etches black/brown in color.

effects of microstructural texturing and grain growth that occurs at high temperatures. Newer detection technologies are developing, and many already exist, which will allow for rapid X-ray detection with areal detectors such as the one used in the CHC diffraction experiments but with higher data-sampling rates. Some of these detectors are already incorporated into third-generation beam lines, and would provide increased ability to monitor welding-induced phase transformations at higher speeds.

If *in-situ* diffraction data are to be taken more rapidly or at higher spatial resolutions, then brighter beams will be required to produce the necessary intensity to accompany smaller integrated X-ray fluxes. Since the current SRXRD and TRXRD setups have not been optimized for brightness, there is plenty of room to grow without taxing existing synchrotron capabilities. For example, third-generation synchrotrons with undulators or more highly focused beams can utilize the full beam's power without having to pass the beam through a pinhole to provide the needed spatial resolution. This preserves all of the beam's intensity, and this effect alone will easily provide orders of magnitude increase to the X-ray photon flux in the weld region. These brighter beams also have higher inherent spatial resolution allowing smaller welds and smaller HAZs to be investigated. As bright as third-generation synchrotrons already are, the next generation of high-energy X-ray sources such as free electron lasers, will provide orders of magnitude brighter beams than those of current synchrotrons (Refs. 1, 3), but is doubtful that such bright beams will be required for *in-situ* welding experiments on anything other than welds with extremely small dimensions.

The future of *in-situ* observations of

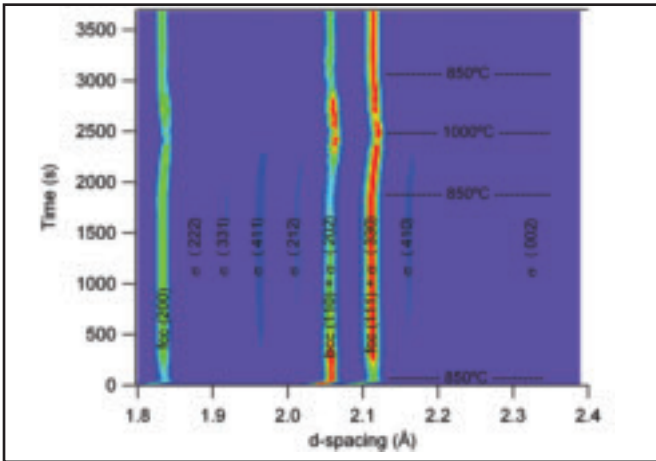


Fig. 21 — In-situ X-ray diffraction sequence up to 3700 s as detected by CHC of a duplex stainless steel alloy where the temperature was ramped to and from 1000°C, after an isothermal hold at 850°C. The sigma phase first appears at a time of 81 s.

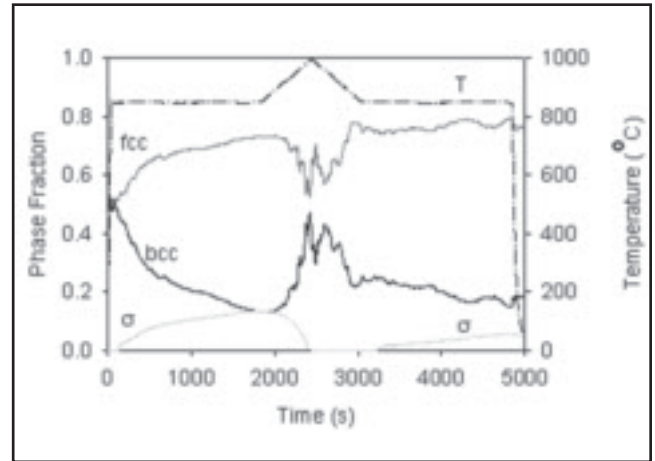


Fig. 22 — Measured fractions of ferrite (bcc), austenite (fcc), and sigma phases in a duplex stainless steel alloy as a function of time as determined by CHC. The temperature profile is indicated by the dashed line. Noise in the ferrite and austenite fractions appear at high temperatures when grain growth occurs and only a few grains satisfy the Bragg condition for diffraction. Both sigma phase formation at 850°C and its dissolution at temperatures approaching 1000°C are captured.

welds is one with a lot of growth potential, and will most likely involve some combination of all of the above effects including brighter synchrotron beams, faster X-ray detectors and new methods for rapidly detecting and mapping the phases that exist during welding. These advances will allow a wider range of welding techniques to be evaluated, for example, laser welding, resistance welding, and friction stir welding. In addition, weld simulation techniques like CHC diffraction can be augmented by incorporating mechanical stressing in addition to heating, so that true thermomechanical behavior of welds can be simulated and analyzed by *in-situ* X-ray diffraction. Furthermore, by incorporating more sophisticated and faster areal X-ray detectors into the experiments, residual stress analysis in real time will become a real possibility. Thinking outside of synchrotrons, the availability of higher flux neutron beams, such as the spallation neutron source at Oak Ridge National Laboratory, will be a big step forward to being able to perform real-time volumetric neutron diffraction and stress analysis on welds or simulated welds in real time, and there should be ample opportunity for new research in this field as well.

Acknowledgments

This work was performed under the auspices of the U.S. Department of Energy by Lawrence Livermore National Laboratory under Contract DE-AC52-07NA27344. Much of this work was supported by DOE, Office of Basic Energy Sciences, Division of Materials Science. Portions of this research were carried out at the Stanford Synchrotron Radiation

Laboratory, a national user facility operated by Stanford University on behalf of the U.S. Department of Energy, Office of Basic Energy Sciences. The UNICAT facility at the Advanced Photon Source (APS) is supported by the U.S. DOE under Award No. DEFG02-91ER45439, through the Frederick Seitz Materials Research Laboratory at the University of Illinois at Urbana-Champaign, the Oak Ridge National Laboratory (U.S. DOE contract DE-AC05-00OR22725 with UT-Battelle LLC), the National Institute of Standards and Technology (U.S. Department of Commerce), and UOP LLC. The APS is supported by the U.S. DOE, Basic Energy Sciences, Office of Science under contract No. W-31-109-ENG-38. Additional portions of the research were performed by The Pennsylvania State University, under grant DE-FGO2-01ER45900. I would like to acknowledge the many collaborators who have worked with me over the past number of years to develop the synchrotron techniques for welding, particularly Professor Suresh Babu, Dr. Todd Palmer, Dr. Eliot Specht, Mr. Phil Waide, and Dr. Joe Wong. In addition, the modeling efforts provided by Professor T. DebRoy and his students at the Pennsylvania State University, Dr. X. He, Dr. Amit Kumar, Mr. Sarang Sista, Dr. Zhishang Yang, and Dr. Wei Zhang have added greatly to the analysis of the experimental results. I would like to also thank the postdoctoral researchers and PhD students at the time, Professor Michael Fröba, Dr. Peter Mayr, Professor Thorsten Ressler, and Dr. Richard Thissen, who have contributed to the analysis of the synchrotron data in many different and helpful ways.

References

1. *Synchrotron Radiation Sources, A Primer*. 1994. Edited by H. Winick, World Scientific.
2. *Handbook on Synchrotron Radiation*. 1983. Vol. 1a, edited by Ernst-Eckhard Koch, North-Holland Publishing Co.
3. *Handbook on Synchrotron Radiation*. 1991. Vol. 3, by G. S. Brown and D. E. Moncton, Elsevier Press.
4. *50 Years of X-Ray Diffraction*, P. P. Ewald editor. Reprinted for the IUCr XVIII Congress, Glasgow, Scotland, Copyright © 1962, 1999 International Union of Crystallography.
5. *The Development of X-ray Analysis*, 1992. William Lawrence, Bragg D. C. Phillips, and H. Lipson, Dover.
6. *X-Ray Data Booklet*. 2001. Lawrence Berkeley National Laboratory, University of California, Berkeley, Calif., second edition, January.
7. Duke, P. J. 2002. *Synchrotron Radiation, Production and Properties*. Oxford Scientific Publications.
8. Wong, J., Elmer, J. W., Waide, P. A., and Larson, E. M. 1994. In-situ X-ray diffraction of an arc weld showing the phase transformations of Ti and Fe as a function of position in the weld. *Adv. X-ray Analysis* 37, p. 479.
9. Elmer, J. W., Wong, J., Fröba, M., Waide, P. A., and Larson, E. M. 1996. Analysis of heat affected zone phase transformations using *in-situ* spatially resolved X-ray diffraction with synchrotron radiation. *Metall. Mater. Trans. A*, v27A(3): 775, 1996.
10. Elmer, J. W., Wong, J., Fröba, M., and Waide, P. A. 1996. An experimental method for investigating phase transfor-

mations in the HAZ of welds using synchrotron radiation. *4th International Conference on Trends in Welding Research*, edited by H. B. Smartt, J. A. Johnson, and S. A. David, ASM International, p. 229.

11. Grong, Ø. 1994. *Metallurgical Modelling of Welding*. The Institute of Materials, London.

12. Easterling, K. 1983. *Introduction to the Physical Metallurgy of Welding*, Butterworths and Co.

13. Kou, S. 2002. *Welding Metallurgy*, 2nd Edition, John Wiley and Sons, Inc.

14. Vander Voort, G. F. 1991. *Atlas of Time-Temperature Diagrams for Irons and Steels*, ASM International.

15. Vander Voort, G. F. 1991. *Atlas of Time-Temperature Diagrams for Non-Ferrous Alloys*, ASM International. G. M. Oprea, J. Szekely, and T. W. Eager. 1986. The role of transient convection in the melting and solidification in the arc weld pools. *Metallurgical Transactions B* 17B: 735–744.

16. Oprea, G. M., and Szekely, J. A. 1987. A comprehensive representation of transient weld pool development in Spot Welding Operations, *Metallurgical Transactions A* 18A: 1325–1332.

17. Zacharia, T., David, S. A., Vitek, J. M., and DebRoy, T. 1989. Weld pool development during GTA and laser-beam welding of type 304 stainless steel: 1. Theoretical analysis. *Welding Journal* 68(12): 499-s to 509-s.

18. Zacharia, T., David, S. A., Vitek, J. M., and DebRoy, T. 1989. Weld pool development during GTA and laser-beam welding of type 304 stainless steel: 2. Experimental correlation. *Welding Journal* 68(12): 510-s to 519-s.

19. Bertram, L. A. 1993. Flow effects on the solidification environment in a GTA spot weld. *Journal of Engineering Materials and Technology* 115: 24–29.

20. Pitscheneder, W., DebRoy, T., Mundra, K., and Ebner, R. 1996. Role of sulfur and processing variables on the temporal evolution of weld pool geometry during multi-kilowatt laser welding of steels. *Welding Journal* 75(3): 71-s to 80-s.

21. Kim, W. H., and Na, S. J. 1998. Heat and fluid flow in pulsed current GTA weld pool. *International Journal of Heat and Mass Transfer* 41: 3213–3227.

22. Wang, Y., and Tsai, H. L. 2001. Effects of surface active elements on weld pool fluid flow and weld penetration in gas metal arc welding. *Metallurgical and Materials Transactions B* 32B: 501–515.

23. Mundra, K., DebRoy, T., and Kelkar, K. 1996. *Numer. Heat Transfer*, Vol. 29, p. 115.

24. Yang, Z., and DebRoy, T. 1999. Modeling macro- and microstructures of gas-metal-arc welded HSLA-A-100 steel. *Metall. Mater. Trans. B* 30B, pp. 483–493,

25. Zhang, W., Roy, G. G., Elmer, J. W., and DebRoy, T. 2003. Modeling of heat transfer and fluid flow during GTA spot welding of 1005 steel. *Journal of Applied Physics* 93(5): 3022–3033.

26. He, X., Fuerschbach, P. W., and DebRoy, T. 2003. Heat transfer and fluid flow during laser spot welding of 304 stainless steel. *Journal of Physics, D: Applied Physics*, 36: 1388–1398.

27. He, X., Fuerschbach, P. and DebRoy, T. 2003. Probing temperature during laser spot welding from vapor composition and modeling. *Journal of Applied Physics* 94(10): 6949–6958.

28. Elmer, J. W., Wong, J., and Ressler, T. 1998. Spatially resolved X-ray diffraction phase mapping and $\alpha \rightarrow \beta \rightarrow \alpha$ transition kinetics in the HAZ of commercially pure titanium arc welds. *Metall. and Mater. Trans. A* 29A(11): 2761–2773.

29. Ressler, T., Wong, J., and Elmer, J. W. 1998. Investigation of real-time microstructure evolution in steep thermal gradients using spatially resolved X-ray diffraction: A case study for Ti fusion welds. *J. Phys. Chem. B* 102(52): 10724.

30. Wong, J., Fröba, M., Elmer, J. W. and Waide, P. A. 1997. In-situ phase mapping and transformation study in fusion welds. *J. Mat. Sc.*, 32, p. 1493.

31. Elmer, J. W., Wong, J., and Ressler, T. 2001. Spatially resolved X-ray diffraction mapping of phase transformations in the HAZ of C-Mn steel arc welds. *Metall. and Mater. Trans. A* 32A(5): 1175–1187.

32. Elmer, J. W., Palmer, T. A., and Wong, J. 2003. In-situ observations of phase transitions in Ti-6Al-4V alloy welds using spatially resolved X-ray diffraction. *Journal of Applied Physics* 93(4): 1941–1947.

33. Palmer, T. A., Elmer, J. W., and Wong, J. 2002. In-situ observations of ferrite/austenite transformations in duplex stainless steel weldments using synchrotron radiation. *Science and Technology of Welding and Joining* 7(3): 159–171.

34. Palmer, T. A., and Elmer, J. W. 2005. Direct observations of the nucleation and growth of austenite from pearlite and allotriomorphic ferrite in a C-Mn steel arc weld. *Scripta Materialia* 53(5): 535–540.

35. Palmer, T. A., and Elmer, J. W. 2005. Direct observations of the $\alpha \rightarrow \gamma$ transformation at different input powers in the heat affected zone of 1045 C-Mn steel arc welds observed by spatially resolved X-ray diffraction. *Metallurgical and Materials Transactions A* 36A: 3353–3369.

36. Elmer, J. W., and Palmer, T. A. 2006. In-situ mapping and direct observations of phase transformations during arc welding of 1045 steel. *Metallurgical and Materials Transactions* 37A(7): 2171–2182.

37. Elmer, J. W., Palmer, T. A., Zhang, W., Wood, B., and DebRoy, T. 2003. Kinetic modeling of phase transformations occurring in the HAZ of C-Mn steel welds based on direct observations. *Acta Materialia* 51: 3333–3349.

38. Kumar, A., Mishra, S., Elmer, J. W., and DebRoy, T. 2005. Optimization of Johnson Mehl Avrami equation parameters for α -ferrite to γ -austenite transformations in steel welds using a genetic algorithm. *Metallurgical and Materials Transactions A* 36A(1): 15–22.

39. Yang, Z., Elmer, J. W., Wong, J., and DebRoy, T. 2000. Evolution of titanium arc weldment macro- and microstructures — Modeling and real time mapping of phases. *Welding Journal* 79(4): 97-s to 112-s.

40. Yang, Z., Sista, S., Elmer, J. W., and DebRoy, T. 2000. Three dimensional monte carlo simulation of grain growth during GTA welding of titanium. *Acta Metall. Mater* 48(12): 4813–4825.

41. Zhang, W., Elmer, J. W., and DebRoy, T. 2005. Integrated modeling of thermal cycles, austenite formation, grain growth and decomposition in the heat affected zone of carbon steel. *Science and Technology of Welding and Joining* 10(5): 574–582.

42. Zhang, W., Elmer, J. W., and DebRoy, T. 2002. Modeling and real time mapping of phases during GTA welding of 1005 steel. *Materials Science and Engineering A* 333(1-2): 321–335.

43. Zhang, W., Elmer, J. W., and DebRoy, T. 2002. Kinetics of ferrite to austenite phase transformation during welding of 1005 steel. *Scripta Materialia* 46: 753–757.

44. Zhang, W., DebRoy, T., Palmer, T. A., and Elmer, J. W. 2005. Modeling of ferrite formation in a duplex stainless steel weld considering non-uniform starting microstructure. *Acta Materialia* 53: 4441.

45. Thiessen, R. G. 2006. Physically based modelling of phase transformations during welding of low-carbon steel. *Materials Science and Engineering A* 427(1-2): 223–231.

46. Karpenko, V., Kinney, J. H., Kulkarini, S., Neufeld, K., Poppe, C., Tirsell, K. G., Wong, J., Cerino, J., Troxel, T., Yang, J., Hoyer, E., Green, M., Humphries, D., Marks, S., and Plate, D. 1989. *Rev. Sci. Instrum.*, Vol. 60, pp. 1451–1456.

47. Bearden, J. A., and Burr, A. F. 1967. *Rev. Mod. Physics*, Vol. 39, p. 125.

48. Babu, S. 2002–2004. Private communications and software code development, Oak Ridge National Laboratory.

49. Elmer, J. W., Palmer, T. A., Babu, S. S., Zhang, W., and DebRoy, T. 2004. Phase transformation dynamics during welding of Ti-6Al-4V. *Journal of Applied Physics*. 95(12): 8327–8339.

50. Elmer, J. W., Palmer, T. A., Babu, S. S., Zhang, W., and DebRoy, T. 2004. Direct observations of austenite, bainite, and martensite formation during arc welding of 1045 steel using time resolved X-ray diffraction. *Welding Journal* 83(9): 244-s to 253-s.
51. Palmer, T. A., Elmer, J. W., and Babu, S. S. 2004. Observations of ferrite/austenite transformations in the heat affected zone of 2205 duplex stainless steel spot welds using time resolved x-ray diffraction. *Materials Science and Engineering A* 374: 307–321.
52. Elmer, J. W., Wong, J., and Ressler, T. 2000. In-situ observations of phase-transformations during solidification and cooling of austenitic stainless steel welds using time-resolved X-ray diffraction. *Scripta Materialia* 43(8): 751–757.
53. Babu, S. S., Elmer, J. W., David, S. A., and Quintana, M. 2002. In-situ observations of non-equilibrium austenite formation during weld solidification of a Fe-C-Al-Mn low alloy steel. *Proceedings of the Royal Society: Mathematical, Physical and Engineering Sciences* Vol. 458: 811–821.
54. Babu, S. S., Elmer, J. W., Vitek, J. M., and David, S. A. 2002. Time-resolved X-ray diffraction investigation of primary weld solidification in Fe-C-Al-Mn steel welds. *Acta Materialia* 50(19): 4763–4781.
55. Wong, J., Ressler, T., and Elmer, J. W. 2003. Dynamics of phase transformations and microstructure evolution in carbon-manganese steel arc welds using time resolved synchrotron X-ray diffraction. *J. Synchrotron Radiation* 10(2): 154–167.
56. Elmer, J. W., Palmer, T. A., Zhang W., and DebRoy, T. 2007. Time resolved in-situ X-ray diffraction observations of phase transformations during arc spot welding. Submitted to the *Science and Technology of Welding and Joining*.
57. Palmer, T. A., and Elmer, J. W. 2007. Direct observation of austenitization in 1005 C-Mn steel during continuous heating using in-situ synchrotron X-ray diffraction. Submitted to *Metallurgical and Materials Transactions A*.
58. Elmer, J. W., Palmer, T. A., and Specht, E. D. 2007. Direct observations of sigma phase formation in duplex stainless steels using in-situ synchrotron X-ray diffraction. *Metallurgical and Materials Transactions A* 38A(3): 464–475.
59. Elmer, J. W., Palmer, T. A., and Specht, E. D. 2007. In-situ observations of sigma phase dissolution in 2205 duplex stainless steel using synchrotron X-ray diffraction. *Materials Science and Engineering A* 459(1-2): 151–155.
60. Elmer, J. W., Palmer, T. A., Babu, S. S., and Specht, E. D. 2005. Low temperature relaxation of residual stress in Ti-6Al-4V. *Scripta Materialia* 52:1051–1056.
61. Elmer, J. W., Palmer, T. A., Babu, S. S., and Specht, E. D. 2005. In-situ observations of lattice expansion and transformation rates of α and β phases in Ti-6Al-4V. *Materials Science and Engineering A*, 391:104–113.
62. Elmer, J. W., Palmer, T. A., and Specht, E. D. 2006. Direct observations of rapid diffusion of Cu in Au thin films using in-situ X-ray diffraction. *Journal of Vacuum Science and Technology-A* 24(4) July/Aug: 978–987.
63. Thissen, R. G. 2006. *Physically-Based Modeling of Materials Response to Welding*. PhD dissertation thesis, Department of Materials Science and Technology, Delft University of Technology, The Netherlands.
64. Thiessen, R. G., Sietsma, J., Palmer, T. A., Elmer, J. W., and Richardson, I. M. 2007. Phase-field modelling and synchrotron validation of phase transformations in martensitic dual-phase steel. *Acta Materialia* 55:601–614.
65. Mayr, P. 2007. *Evolution of microstructure and mechanical properties of the heat affected zone in B-containing 9% chromium steels*. PhD dissertation thesis, Graz University of Technology, Austria.
66. Mayr, P., Palmer, T. A., Elmer, J. W., and Cerjak, H. 2007. In-situ observations of phase transformations and their effects in 9–12% Cr steels during welding. *Trans Tech Publications, Advanced Materials Research*, Vols. 15–17, pp. 1014–1019.
67. Mayr, P., Palmer, T. A., Elmer, J. W., and Specht, E. D. 2007. Direct observations of phase transformations in the simulated heat-affected-zone of a 9%Cr martensitic steel. Submitted to the *International Journal of Materials Research*.
68. Hammersley, A. P. 1998. FIT2D V9.129 Reference Manual V3.1, *ESRF Internal Report*, ESRF98HA01T.
69. Hammersley, A. P., Svensson, S. O., Hanfland, M., Fitch, A. N., and Häusermann, D. 1998. *High Pressure Research*, Vol. 14, pp. 235–248.
70. Patankar, S. V. 1980. *Numerical Heat Transfer and Fluid Flow*. Hemisphere Pub. Corp.
71. Sundman, B., Jansson, B., and Andersson, J. 1985. *Calphad-Computer Coupling of Phase Diagrams and Thermochemistry* 9(2): 153.
72. JPOWD: Materials Data Inc., Livermore, Build 11/17/2005.
73. Elmer, J. W., Allen, S. M., and Eagar, T. W. 1989. Microstructural development during solidification of stainless steel alloys. *Metall. Trans. A* 20A(10): 2117–2131.
74. Wong, J., Waide, P. A., Elmer, J. W., and Thompson, A. C. 2000. Spatially resolved diffraction using a soler collimator-imaging plate assembly. *Nucl. Instrum. Meth. A*, 446(3): 581–591.

Call for Papers

15th Int'l Conf. on the Joining of Material

The 15th International Conference on the Joining of Materials (JOM-15) and the 6th International Conference on Education in Welding (ICEW-6) Conference and Exhibition organized by JOM Institute and supported by Dansk Metal, Danish Welding Society, and DSL FORCE Technology, will be held May 3–6, 2009, Helsingør, Denmark.

A full technical program on welding technology and education and training will be conducted. The main topics are listed below.

1) Recent developments in joining technology — welding, soldering, brazing, and projects, with the emphasis on industrial applications,

2) Welding quality — properties and environmental considerations,

3) Welding management and qualification of welding personnel.

The organizers cordially invite you to send a title of your presentation and a short abstract by October 15, 2008. Notification of acceptance and author's guidelines will follow after review of the abstracts by December 2008. Full papers must be received by February 2009. Please send your name, address, title, and abstract to: Alan Parnes (Dansk Metal). e-mail alan.parnes@danskmetal.dk. For further information about the conference contact JOM. Gilleleje Strandvej, 28. DK-3250 Gilleleje. Denmark. Telephone: +45 48355458, e-mail jom_aws@post10.tele.dk.